1

2

Deamidation disrupts native and transient contacts to weaken the interaction between UBC13 and RING-finger E3 ligases

5

6 **Priyesh Mohanty[1], Rashmi[1], Batul Ismail Habibullah[1], Arun G S[1], and Ranabir Das[1,2]**

7 [1]National Centre for Biological Sciences, Tata Institute of Fundamental Research, Bengaluru-

8 560065, India

9

10

11

12

13

14

15

16

17

18

19

20

21
22 **[2] Correspondence to:**
23 R. D. (rana@ncbs.res.in)
24

1

25
26 **Abstract**

27 The deamidase OspI from enteric bacteria *Shigella flexneri* deamidates a glutamine residue in the

28 host ubiquitin-conjugating enzyme UBC13 and converts it to glutamate (Q100E). Consequently, its

29 polyubiquitination activity in complex with the RING-finger ubiquitin ligase TRAF6 and the downstream

30 NF-κB inflammatory response is inactivated. The precise role of deamidation in inactivating the

31 UBC13/TRAF6 complex is unknown. We report that deamidation inhibits the interaction between

32 UBC13 and TRAF6 RING-domain (TRAF6^{RING}) by perturbing both the native and transient

33 interactions. Deamidation creates a new intramolecular salt-bridge in UBC13 that competes with a

34 critical intermolecular salt-bridge at the native UBC13/TRAF6^{RING} interface. Moreover, the salt-bridge

35 competition prevents transient interactions necessary to form a typical UBC13/RING complex.

36 Repulsion between E100 and the negatively charged surface of RING also prevents transient

37 interactions in the UBC13/RING complex. Our findings highlight a mechanism where a post-

38 translational modification perturbs the conformation and stability of transient complexes to inhibit

39 protein-protein association.

40

41

42

43

44

45

2

Introduction

47 Several bacterial pathogens secrete effector proteins that inhibit or co-opt the Ubiquitin (Ub) pathway

48 to suppress the immune response of the host cell (Ashida, Kim & Sasakawa 2014). The human

49 pathogenic bacteria *Shigella flexneri* inactivates the host inflammatory Nf-κB signaling, responsible for

50 inducing inflammatory cytokine responses during pathogen invasion (Sanada et al. 2012). In the early

51 events of interleukin-dependent activation of Nf-κB signaling, the Ub-conjugating enzyme UBC13, and

52 the Ub-ligase TRAF6 function together to synthesize both unanchored polyubiquitin chains, and

53 anchored polyubiquitin chains on TRAF6 and its substrate NEMO (Chen 2005). These chains serve as

54 a scaffold to bring together TAK1/2 and IKK kinases, eventually leading to phosphorylation and

55 activation of the IKK kinases, IκB degradation and nuclear translocation of transcription factor Nf-κB.

56 To inactivate Nf-κB signaling, *Shigella flexneri* secretes a Type III effector called OspI, which functions

57 as a deamidase (Sanada et al. 2012). OspI specifically targets a glutamine residue in UBC13 and

58 converts it to glutamate (Q100E). Ubiquitination reactions of TRAF6 either with UBC13 in the

59 presence of OspI or with mutant Q100E-UBC13 (dUBC13) show a significant drop in

60 polyubiquitination activity (Sanada et al. 2012). However, the mechanism underlying inhibition of

61 polyubiquitination by deamidation of UBC13 remains unclear.

62 Ubiquitination is a eukaryotic post-translational modification (Komander & Rape 2012),

63 wherein the last glycine residue in the C-terminal tail of Ubiquitin (Ub) is activated and covalently

64 attached to a substrate lysine residue. Ubiquitination involves three steps: an initial activation and

65 thioester conjugation by the Ubiquitin-activating enzyme (E1), followed by the thioester conjugation to

66 the Ubiquitin-conjugating (E2) enzymes, and a final step in which the Ub is covalently attached to the

67 substrate amino group. The last step is typically catalyzed by a class of Ubiquitin ligases (E3), which

68 contain either a RING(Really Interesting New Gene)-finger domain, U-box domain or HECT domain

69 (Metzger et al. 2010). The RING-finger/U-box domain stabilizes a catalytic-closed conformation of the

70 flexible E2~Ub species and drastically enhances the rate of Ub conjugation to substrates (Dou et al.

71 2012; Plechanovov et al. 2012; Pruneda et al. 2012). The E2 UBC13 functions with several RING-

3

72   finger E3s like TRAF6 to synthesize K63-linked poly-Ub chains that function to activate DNA repair or

73   immune response (Matsuzawa et al. 2007). Apart from the E3s, UBC13 also binds a co-factor MMS2,

74   which does not activate UBC13 but maintains the linkage specificity of the poly-Ub chains synthesized

75   by UBC13 (Branigan et al. 2015).

76   In this study, we have investigated the mechanisms underlying the inactivation of UBC13

77   upon deamidation using NMR spectroscopy, molecular dynamics (MD) simulations, and *in-vitro*

78   ubiquitination assays. We report that deamidation weakens the non-covalent interaction of UBC13

79   with RING-finger domain of TRAF6 (TRAF6^{RING}), without perturbing UBC13 structure or the enzymatic

80   activity of UBC13. However, the underlying cause of reduced interaction is nonintuitive since Q100 is

81   in the vicinity of UBC13/TRAF6^{RING} interface but does not form any contact with the TRAF6^{RING}.

82   Further studies showed that deamidation disrupts the interaction between UBC13 and TRAF6^{RING} by

83   three mechanisms: i) A new intramolecular R14/E100 salt-bridge appears in dUBC13, which competes

84   with a critical intermolecular salt-bridge in the native complex, ii) the salt-bridge competition also

85   perturbs the UBC13/TRAF6^{RING} transient complexes to inhibit association, and iii) repulsion between

86   the negatively charged E100 and the negatively charged interface of TRAF6^{RING} perturbs the transient

87   complexes to reduce association between UBC13 and TRAF6^{RING}. The effect of each mechanism on

88   the binding was confirmed by binding studies using appropriate substitutions in either UBC13 or

89   TRAF6^{RING}. The impact of deamidation on transient interactions was also observed using another

90   RING domain from RNF38, indicating that the mechanism could be ubiquitous for UBC13/RING

91   complexes. Our study highlights that deamidation of residues that do not directly participate in the

92   E2/E3 interaction but are close to the interface can effectively modulate the interaction by perturbing

93   the native and transient intermolecular contacts. The mechanism of regulating protein-protein transient

94   interactions by post-translational modifications could be at play in other quintessential signaling

95   pathways.

96

4

Results

Deamidation abolishes the interaction between UBC13 and TRAF6^{RING}

Two different constructs of TRAF6 was used in this study. The isolated RING domain TRAF6^{RING} (aa: 50-124) was the shorter construct, while the longer construct included the RING domain and three ZF domains (TRAF6^{RZ3}, aa: 50-211). By the three dimensional structures, TRAF6^{RING} interacts with UBC13 and with the donor Ub in the UBC13~Ub conjugate, while the interaction of ZF domains with donor Ub further stabilizes the UBC13~Ub/TRAF6^{RZ3} complex (Middleton et al. 2017a). Both the E2/E3 complex of dUBC13/TRAF6^{RZ3} and dUBC13/TRAF6^{RING} had reduced polyubiquitination activity than the corresponding wild-type complexes (Figure 1A, 1B). Deamidation could have some allosteric effect at the active site or Ub-binding site, which may deactivate UBC13. However, a comparison of the extent of polyubiquitination by the UBC13/MMS2 heterodimer in the absence of E3 was similar between UBC13 and dUBC13, indicating that E2 activity is not altered upon deamidation (Figure 1C).

Deamidation could misfold UBC13 or inhibit the interaction between UBC13 and TRAF6^{RING}. These possibilities were examined by studying the impact of deamidation on the structure of UBC13 and its interaction with TRAF6^{RING}. ^{15}N-labeled UBC13/dUBC13 and unlabelled TRAF6^{RING} were expressed in *E. Coli* and purified. Unlabelled TRAF6^{RING} was titrated into a sample of ^{15}N-UBC13, and the binding was detected by ^{15}N-edited Heteronuclear Single Quantum Coherence (HSQC) NMR experiments (Figure S1A). Perturbations due to the altered chemical environment upon ligand binding induce changes in the chemical shift of the backbone amide resonances. The chemical shift perturbations (CSP) plotted in Figure 1D shows that the significant perturbations in UBC13 occur in the α1-helix, and the loop between α$_{3-10}$ and α2-helix, which is the canonical interface of UBC13/TRAF6^{RING} complex (Figure 1G, 1H). The resonance shifts can be plotted against the ligand: protein concentration, and fit to yield the K_d of interaction. The peak shifts in UBC13 titration spectra were fitted to yield a K_d of 0.39 (±0.04) mM (Figure 1I and S1B).

5

121 Backbone amide chemical shifts can report if the protein's structure is affected by the

122 substitution/modification of a residue. The backbone chemical shifts of UBC13 and dUBC13

123 resonances were assigned using ^{13}C, ^{15}N labeled samples, and standard triple resonance NMR

124 experiments. The CSPs between UBC13 and dUBC13 indicated that apart from the residues

125 immediately next to Q100 in sequence, only R14 and L15 of the N-terminal α1-helix are affected upon

126 Q100E substitution (Figure S2A). The absence of major CSPs in the rest of dUBC13 indicated that

127 deamidation did not change the fold of UBC13. Moreover, analysis of the backbone and C_β chemical

128 shifts in dUBC13 confirmed that the secondary structure was unperturbed (Figure S2B). Unlabelled

129 TRAF6^{RING} was then titrated into a sample of ^{15}N-dUBC13, and the binding was detected by ^{15}N-edited

130 HSQC experiments (Figure S3). Negligible peak shifts were detected in dUBC13 even when the

131 TRAF6^{RING} was titrated up to 6-fold higher than dUBC13, indicating that TRAF6^{RING} does not bind

132 dUBC13 (Figure 1E-H, S3B). A rough estimate of the K_d was obtained by comparing the CSPs at the

133 UBC13 interface at the same protein: ligand concentration between UBC13 and dUBC13, which

134 suggested the K_d of 6.34 (±2.6) mM. If the reduced affinity is precisely due to the negative charge at

135 residue 100, then substitution of Q100 with a neutral amino acid should not affect the affinity of the

136 complex. TRAF6^{RING} was titrated to Q100A-UBC13, and the measured K_d was 0.54 (±0.07) mM

137 (Figure 1I), which is similar to UBC13/TRAF6^{RING}. However, when Q100 was substituted with another

138 acidic residue aspartate (D), the affinity dropped significantly (Kd ~ 4.6 (±1.8)) mM, Figure 1I),

139 confirming that substitution at Q100 with a negatively charged residue inhibited the interaction

140 between UBC13 and TRAF6^{RING}. Altogether, deamidation inhibited the binding of TRAF6^{RING} to

141 UBC13, but neither changed the fold of UBC13 nor its intrinsic enzymatic activity.
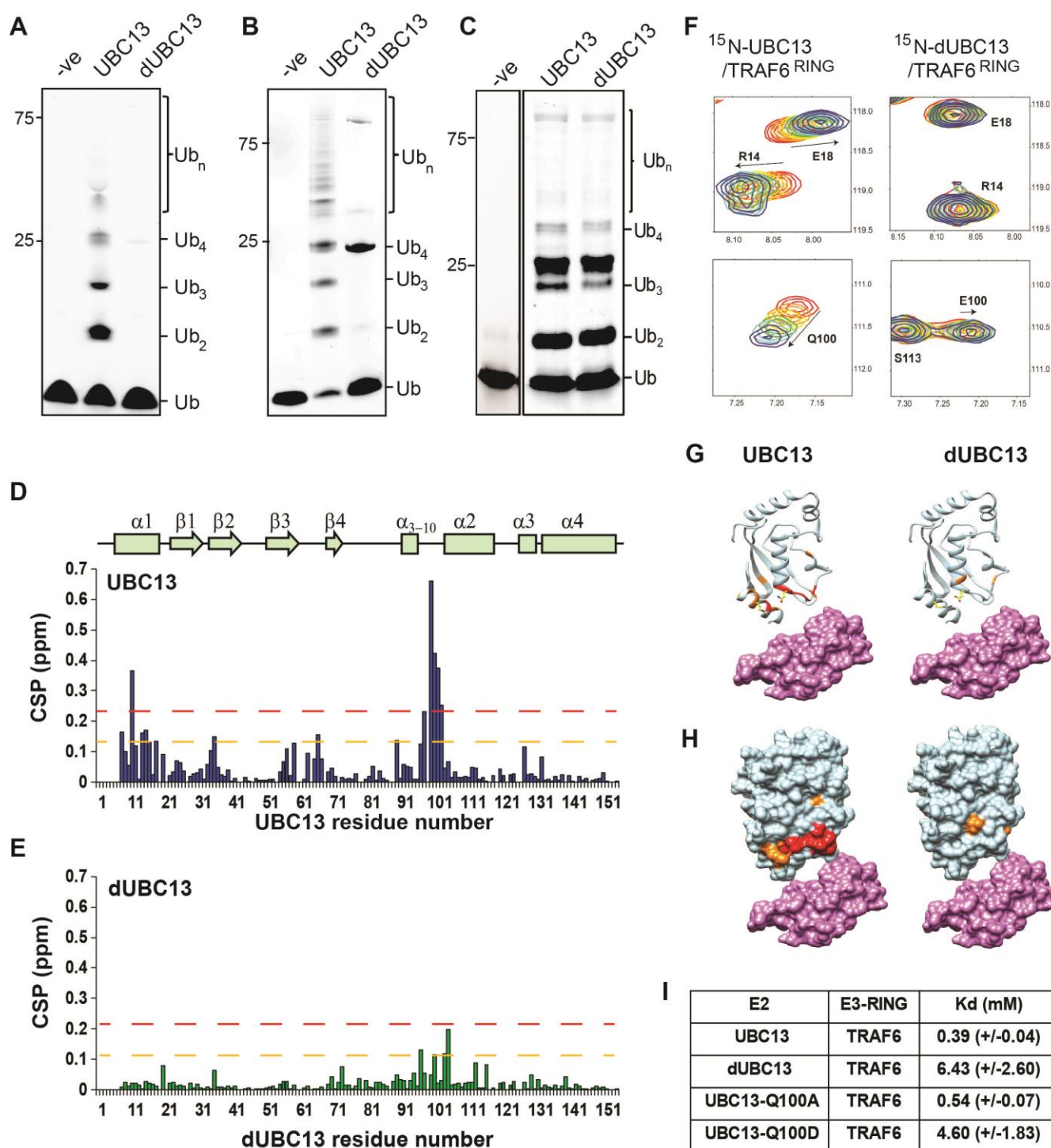
142

143

Figure 1. Interactions between UBC13 and TRAF6^{RING} studied by NMR. A) *In-vitro* ubiquitination reaction was carried out using TRAF6^{RZ3} as the E3 and UBC13 or dUBC13 as the E2 for 10 min. Mms2 was used as a co-factor in the reaction. The –ve lane is the same reaction without ATP. B) *In-vitro* ubiquitination reaction was carried out on GST beads for 10 min using GST-TRAF6^{RING} as the E3 and UBC13 or dUBC13 as the E2. Mms2 was used as a co-factor in the reaction. The –ve lane is the same reaction without ATP. B) *In-vitro* ubiquitination reaction carried out for 30 min using UBC13 or

7

152 dUBC13 as the E2 and Mms2 as its co-factor. C)The CSPs for residues in UBC13 upon binding to

153 TRAF6^{RING}. The chemical shift perturbations (CSP) between the free and the bound form are

154 calculated as CSP = $[(\delta^H_{free} - \delta^H_{bound})^2 + ((\delta^N_{free} - \delta^N_{bound}))^2]^{1/2}$, where δ^H and δ^N is the chemical shift of

155 the amide hydrogen and nitrogen, respectively. The orange and red dashed lines correspond to

156 Mean+SD and Mean+2*SD, respectively. The secondary structure alignment of UBC13 against its

157 sequence is provided above the plot. D) The CSPs for residues in dUBC13 upon binding to

158 TRAF6^{RING}. The dashed lines are replicated from B). E) Two regions of the titration HSQC spectra are

159 expanded to show UBC13, but not dUBC13 peaks shift upon titration with TRAF6^{RING}. Significant

160 CSPs were mapped on the UBC13 and dUBC13 structure both in the F) ribbon and G) surface

161 representation. The UBC13 and dUBC13 are colored in light blue. The residues with CSPs above

162 Mean+SD and Mean+2*SD are colored in orange and red, respectively. The surface of TRAF6^{RING}

163 domain shown in magenta. The UBC13/TRAF6^{RING} complex is modeled from PDB 3HCU. H) The

164 measured dissociation constants of UBC13 and its mutants with TRAF6^{RING} are provided as Mean+/-

165 SD.

166

167 **Deamidation triggers the formation of an intramolecular salt-bridge in UBC13**

168 In the UBC13/TRAF6^{RING} native complex structure, Q100 does not form any contact with TRAF6^{RING}

169 (Figure 2A). Hence, the mechanism underlying reduced binding due to deamidation of Q100 is

170 nonintuitive. The surface electrostatic potentials calculated for UBC13 and TRAF6^{RING} indicated

171 charge complementarity at the interface (Figure 3A). The UBC13 interface was positively charged,

172 while the TRAF6^{RING} was negatively charged. Notably, Q100 lies in the vicinity of a network of

173 electrostatic interactions involving helix-1 of UBC13 (R6 and R14) and the first zinc-coordination motif

174 (D57 and E69) of the TRAF6^{RING} (Figure 2A). Possibly, the introduction of an additional negative

175 charge upon deamidation could perturb the interfacial electrostatic contacts to disrupt the interaction.

176 A conventional MD simulation (200 ns) of free dUBC13 was performed to investigate if

177 deamidation alters any electrostatic interactions within UBC13. Interestingly, an intramolecular salt-

178 bridge was observed between R14 and E100 in dUBC13 (Figure 2B), which correlates well with the

179 backbone chemical shifts observed at R14 upon deamidation (Figure S1B). The formation of the new

180 salt-bridge involving R14 and E100 in dUBC13 was further investigated by NMR spectroscopy. ^{15}N-

181 edited HSQCs of the Arginine Nϵ-Hϵ groups were collected for both UBC13 and dUBC13, which

182 showed shifted resonances for the arginine sidechains (R7, R14, and R102) around residue E100,

183 indicating that these sidechain conformations are perturbed (Figure 2C). Unfortunately, the ^{1}Hη atoms

184 are invisible in the NMR spectra due to chemical exchange with the solvent at physiological pH, and

185 millisecond timescale rotations around the Cζ-Nη/ Cζ-Nϵ bonds (Figure 2D). Hence, detection of

186 arginine sidechain-mediated interactions (hydrogen bonds and salt-bridges) through ^{1}Hη atoms is

187 difficult. However, such interactions can be inferred from the reduced mobility of their sidechains

188 observed in ^{15}Nη/ϵ(F1)-^{13}Cζ(F2) correlation spectra (Yoshimura et al. 2017). For example, R85 forms

189 salt-bridge with D81 in UBC13, which reduces the sidechain mobility of R85 sidechain and gives rise

190 to two separate resonances for R85 Nη atoms in the ^{15}Nϵ/η-^{13}Cζ correlation spectra (Figure 2E). The

191 side-chains of free arginines rotate faster and their corresponding Nη atoms have a single averaged

9

192   resonance in the spectra (Figure 2E). The R14 Nη atoms had two separate resonances in dUBC13

193   but not UBC13 (Figure 2F, expanded in 2G), implying that R14 forms a salt-bridge in dUBC13,

194   consistent with the MD simulations. The salt-bridge persisted in the Q100D-UBC13 (Figure S4),

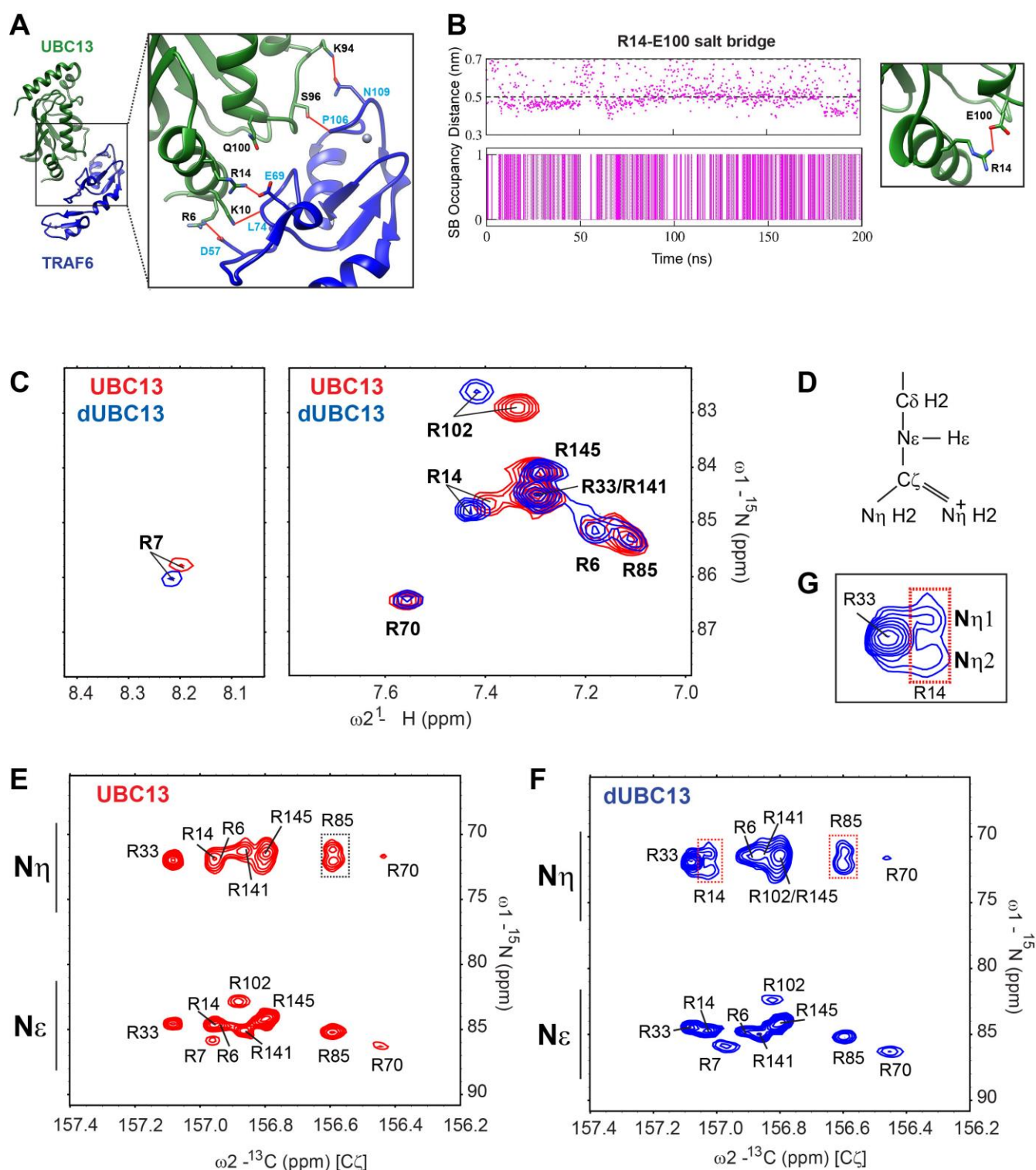195   correlating well with its reduced affinity for TRAF6^{RING}.

196

10

Figure 2: A new intramolecular salt-bridge forms upon deamidation of UBC13. A) Crystal structure of the UBC13/TRAF6[RING] complex (PDB 3HCU, Left). Inset (right) indicates the position of Q100 and the network of salt-bridges/hydrogen bonds (red connecting lines) at the interface of UBC13/TRAF6[RING] complex. B) The distance between R14-Cζ and E100-Cδ atoms against time in the conventional MD simulation of dUBC13 is given (top). The presence/absence of a salt-bridge based

11

204   on a 0.5 nm cutoff value are digitized to a Markov chain, where the presence of a salt-bridge is 1 and

205   absence is 0. C) Overlay of UBC13 and dUBC13 ^{15}N-^{1}H HSQC spectra zoomed around the Arginine

206   Nε-Hε resonances, shows that R7, R14, and R102 sidechain resonances shift upon deamidation. D)

207   Schematic of Arginine sidechain atoms. E) and F) are the ^{15}Nε/η-^{13}Cζ correlation spectra for UBC13

208   and dUBC13, respectively. The ^{15}Nε/η and ^{13}Cζ resonance shifts are in the x- and y-axis, respectively.

209   The R33 and R14 ^{15}Nη resonances of dUBC13 are expanded in G).

210

12

Deamidation triggers salt-bridge competition at the UBC13-TRAF6^{RING} interface

At the interface of UBC13/TRAF6^{RING}, R14 of UBC13 forms an intermolecular salt-bridge with E69 of TRAF6^{RING} (Figure 2A). MD simulations of dUBC13 suggested that the deamidation-induced intramolecular R14/E100 salt-bridge may interfere with the intermolecular R14/E69 salt-bridge to destabilize the complex. Conventional MD simulations were performed with both UBC13/TRAF6^{RING} and dUBC13/TRAF6^{RING} to test this hypothesis. The stability of the complex during the simulation was determined by the rmsd of TRAF6^{RING} with respect to the crystal structure. Higher rmsd implied lower stability of the complex. The UBC13/TRAF6^{RING} complex was stable throughout (Figure S5A). The dUBC13/TRAF6^{RING} complex was unstable for a significant duration in a trajectory, wherein the rmsd of TRAF6^{RING} increased substantially (Figure S5B).

Five interfacial contacts were chosen as the reporter of the interaction between UBC13 and TRAF6^{RING} (Figures S5). The three selected electrostatic contacts were the R14/E69 salt-bridge, R6/D57 salt-bridge, and S96/P106 hydrogen bond (Figure 2A and S5A). The two selected hydrophobic interactions were R7/I72 and M64/L74 (Figure S5D). The other interfacial contacts were mostly unstable in simulations and were omitted from our analysis (Figure S5G and S5H). No major instability was observed in the hydrophobic contacts between UBC13 and dUBC13 (Figure S5E and S5F). However, concurrent to the high rmsd in dUBC13/TRAF6^{RING} complex, the R14/E69 intermolecular salt-bridge disrupted and the R14/E100 intramolecular salt-bridge formed, suggesting a role of the salt-bridge competition in destabilizing the native complex (Figure S5B).

The Umbrella Sampling (US) method was used to determine the change in binding free energy of the UBC13/TRAF6^{RING} complex upon deamidation. The US method quantifies the amount of work done to form the native complex from a distant separation, where the two proteins are non-interacting. The potential of mean force (PMF) for the association between the proteins is computed as a function of their center of mass (COM) separation. As a control of the protocol, US simulations were performed to study the association between Barnase and Barstar (Figure S6, Table 1 and Table S1). The

13

236 observed PMF profile and ΔG_{PMF} (-12.6 kcal mol^{-1}) of the Barnase/Barstar complex are consistent with

237 the high-affinity of the complex (K_d~136 fM) and previous MD studies (Hoefling & Gottschalk 2010;

238 Wang et al. 2010).

239   Destabilizing modifications/substitutions in UBC13 will increase the overall work done (ΔG_{PMF}) to

240 form the native complex. The US simulations were carried out for both the UBC13/TRAF6^{RING} and

241 dUBC13/TRAF6^{RING} complexes (Figure 3B, Table 1, and Table S1). At the 3.2 nm COM separation,

242 the PMF profile of UBC13/TRAF6^{RING} decreased sharply by 2.0 kcal mol^{-1} and subsequently plateaued

243 (Figure 3B). In contrast, ΔG_{PMF} of dUBC13/TRAF6^{RING} gradually reduced by only 0.7 kcal mol^{-1},

244 suggesting that deamidation reduces the binding energy between UBC13 and TRAF6^{RING}. The

245 difference in ΔG_{PMF} between the deamidated and wild-type (wt) complex was in good agreement with

246 the decrease in binding energy observed in the NMR titrations ($\Delta\Delta G_{PMF}$ =1.4 kcal mol^{-1}, $\Delta\Delta G_{binding}$=1.6

247 kcal mol^{-1}). The ΔG_{PMF} of Q100A-UBC13/TRAF6^{RING} is, however, similar to the wt complex (Table 1).

248 **Table 1. Association PMF determined by Umbrella sampling MD.**

Complex	$<\Delta G_{PMF}>$ (kcal mol^{-1})
Barstar/Barnase	-12.60 (±0.76)
UBC13/TRAF6	-2.03 (±0.27)
dUBC13/TRAF6	-0.67 (±0.50)
Q100A-UBC13/TRAF6	-1.64 (±0.49)
R14A-UBC13/TRAF6	+0.04 (±0.38)

259 *Standard error of mean is indicated in brackets

261   The stability of the intermolecular contacts could be compared between the two complexes within

262 the native window in the US simulations. While the R14/E69 salt-bridge was stable throughout in

263 UBC13/TRAF6^{RING}, it disrupted within 4ns due to salt-bridge competition in dUBC13/TRAF6^{RING}

264 (Figure 3C, 3D). The instability of R14/E69 salt-bridge correlates well with lower Coulombic Interaction

265 Energy (CIE) and higher rmsd of TRAF6^{RING} (Figure 3E and 3G). A significant difference of ~30 kcal

266 mol^{-1} was observed in the mean CIE between the two complexes (Figure 3F). In contrast, the

14

267   difference in Lennard-Jones interaction energy was mere ~2.4 kcal mol^{-1}, suggesting that deamidation

268   primarily inhibits the electrostatic interactions. Moreover, the PMF profile of R14A-UBC13/TRAF6^{RING}

269   was flat with ΔG_{PMF}~0 kcal mol^{-1}, suggesting that the interactions mediated by R14 are essential for

270   the complex (Figure 3B). Overall, the native complex simulations and US simulations indicate that

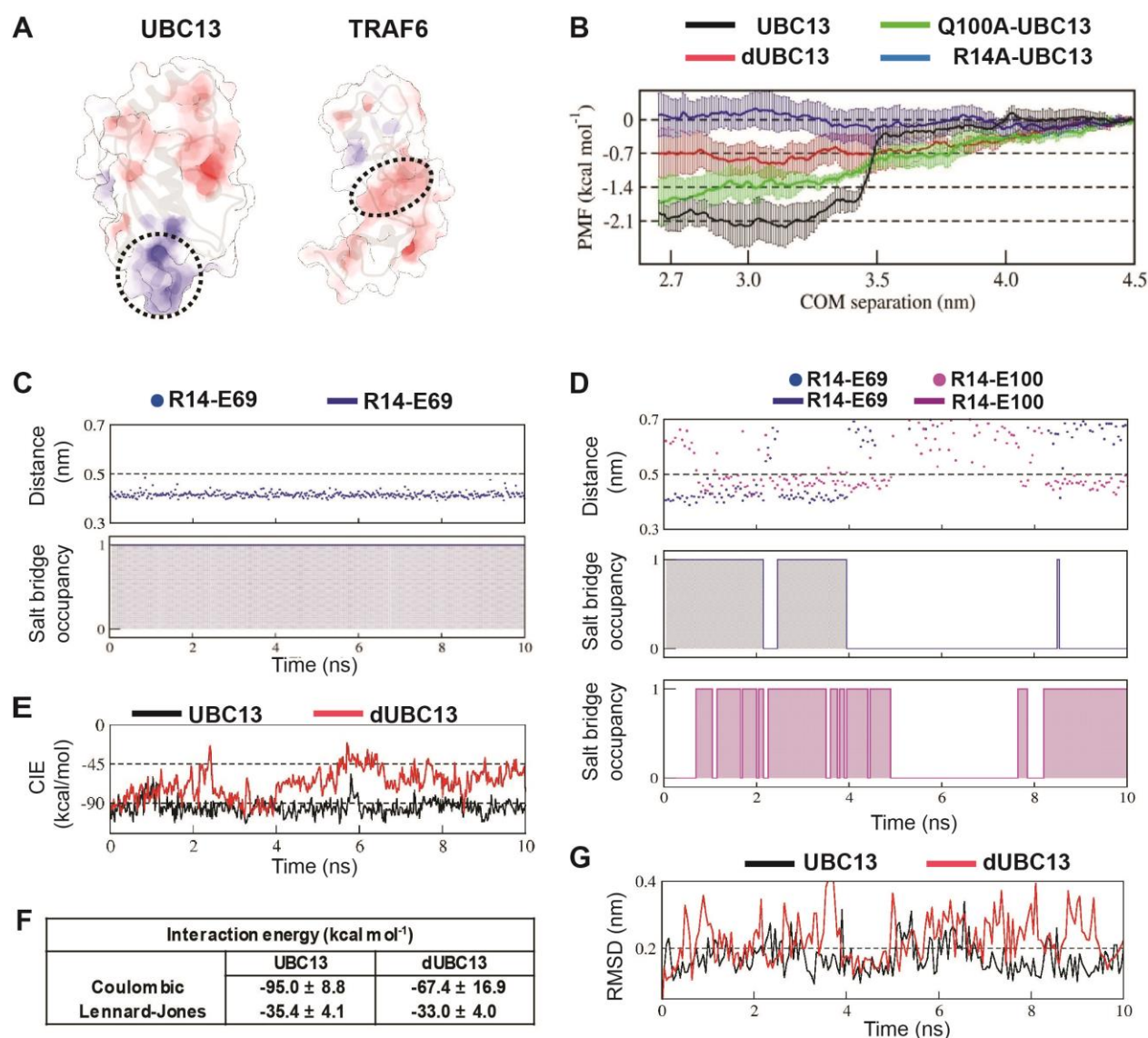271   salt-bridge competition reduces the binding energy of the dUBC13/TRAF6^{RING} complex.

272

Interaction energy (kcal mol^{-1})		
	UBC13	dUBC13
Coulombic	-95.0 ± 8.8	-67.4 ± 16.9
Lennard-Jones	-35.4 ± 4.1	-33.0 ± 4.0

273

274 **Figure 3. Deamidation induces salt-bridge competition to weaken UBC13/TRAF6^{RING} interaction.**

275   A) Surface electrostatic potentials of UBC13 and TRAF6^{RING}. Circled regions indicate the

276   complementary electrostatic surfaces on UBC13 and TRAF6^{RING} interfaces. The color scale ranges

277   from -8 to +8 kT/e. B) Potential of mean force (PMF) profiles as a function of COM separation along

15

278   the x-axis for the association between UBC13 variants and TRAF6^{RING}. PMF profiles were calculated

279   by averaging over five PMF profiles ranging from 2.5 ns to 10 ns. Error bars represent ± one standard

280   error of the mean (SEM). C) Stability and occupancy of the R14-E69 salt-bridge in the native window

281   for the wild-type complex. D) Stability and occupancy of the R14-E69 and R14-E100 salt-bridge in the

282   native window for the dUBC13/ TRAF6^{RING} complex. In C) and D), distance plots indicate the distance

283   between R14 Cζ and E69/E100 Cδ atoms. The salt-bridge occupancy plots were generated as in

284   Figure 2B. E) Coulombic interaction energies (CIE) between UBC13 wild-type/Q100E and TRAF6^{RING}

285   in native windows (mean COM separation = 2.7 nm) from the US simulations. The table in (F) reports

286   the Mean ± SD of the interaction energies over 10 ns. G) RMSD of TRAF6^{RING} (aa:70-109) against

287   time in the UBC13 and dUBC13 complexes.

288

16

Salt-bridge competition enhances the dissociation of dUBC13/TRAF6^{RING}

290   To capture the effects of deamidation on the dissociation of the native complex, steered MD (SMD)

291   simulations were performed for both the wt and dUBC13 complex. Ten independent, 30 ns long SMD

292   simulations were performed, wherein the COM of the TRAF6^{RING} was separated from UBC13 by ~6

293   nm at a slow rate of 0.125 nm ns^{-1}. The COM position of UBC13 was kept fixed. The average

294   maximum unbinding force (F_{max}) and work (W) profiles were determined by combining all SMD

295   simulations (Figure 4A, B and Table 2). The distribution of F_{max} and W for individual SMD trajectories

296   are given in Figure 4C and Table S2. Compared to the UBC13/TRAF6^{RING} complex, lesser F_{max} and W

297   were required to dissociate the dUBC13/TRAF6^{RING} complex, indicating reduced stability due to

298   deamidation of UBC13. The mean occupancy of the R14/E69 salt-bridge was lower for

299   dUBC13/TRAF6^{RING} compared to UBC13/TRAF6^{RING} (Figure 4D, S7, S8), because the salt-bridge

300   competition disrupted the R14/E69 salt-bridge for prolonged periods in several trajectories (Figure S8 -

301   trajectories 3,4,5 & 9). As a result, the W of these trajectories were lower than the minimum value of W

302   (28 kcal.mol^{-1}) observed in any wt trajectory (Table S2). A similar destabilization of the complex was

303   observed when the SMD was repeated with R14A-UBC13, where the R14/E69 salt-bridge is absent.

304   Overall, R14/E69 salt-bridge was unstable in the dUBC13/TRAF6^{RING} complex, which reduced the

305   unbinding work required to dissociate the complex.

306   The order in which the contacts disrupted during dissociation was compared in a typical SMD

307   trajectory for both complexes (Figure 5A and Movies S2, S3). Whereas the other significant contacts

308   disrupted within 8 ns, the R14/E69 salt-bridge persisted till the complex dissociated completely at 15

309   ns (Figures 5A-5C and S9). Given the R14/E69 salt-bridge was stable in both conventional and SMD

310   simulations, it could be critical for the stability of the wt complex. On the contrary, R14/E69 salt-bridge

311   disrupted within 3 ns in the dUBC13/TRAF6^{RING} complex, due to competition from the R14/E100 salt-

312   bridge (Figures 5D-F). The R14/E100 salt-bridge in dUBC13 remained stable after dissociation of

313   TRAF6^{RING} (Figure 5E). Collectively, the SMD suggested that R14/E69 formed a critical interfacial salt-

314   bridge, and competition from E100 disrupted the salt-bridge to enhance dissociation of the complex.

17

Table 2. F_{max} and unbinding work determined by Steered MD.

Complex	<F_{Max}> (pN)	<Work> (kcal mol^{-1})
UBC13/TRAF6	466.7 (±31.5)	38.1 (±2.2)
dUBC13/TRAF6	425.9 (±42.2)	29.6 (±1.6)
R14A-UBC13/TRAF6	450.4 (±45.9)	31.9 (±2.1)

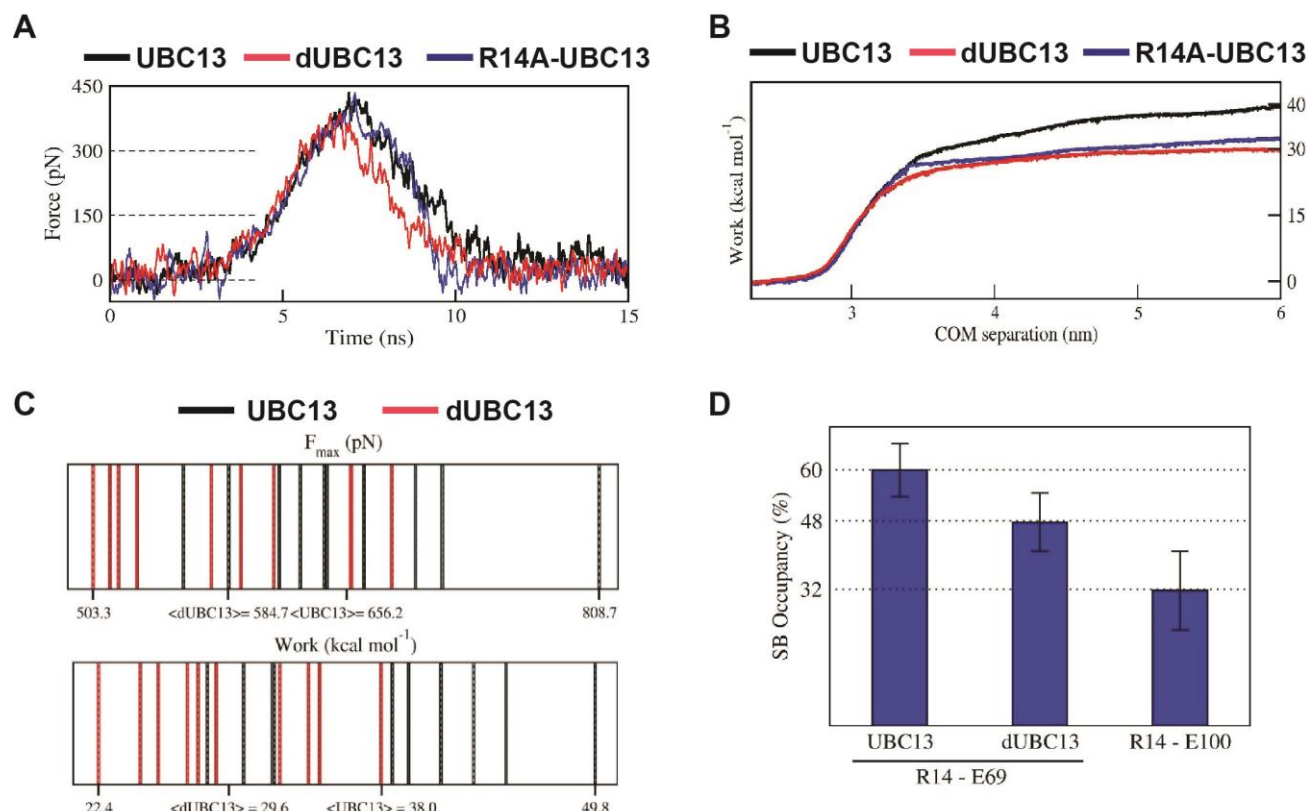*Standard error of mean is indicated in brackets

Figure 4. Steered MD of the UBC13/TRAF6^{RING} and dUBC13/TRAF6^{RING} complex. A) Average force-extension profiles for wild-type and mutant complexes are plotted. The profiles were smoothened over 250 ps time intervals. B) The plot of average work against COM separation indicated the cumulative work done to separate wild-type and mutant complexes. C) Distribution of F_{max} (top) and unbinding work (bottom) values obtained from ten individual SMD trajectories for wild-type (black) and mutant (red) complexes are shown. In each plot, the minimum, maximum, and average (< >) values are indicated on the x-axis. Both plots reveal a shift in the range of F_{max} and unbinding work towards lower values for the dUBC13/TRAF6^{RING} complex, which correlate with the reduced binding. D) Mean ± one standard error (SEM) of R14-E69/E100 salt-bridge (SB) occupancies

18

331 averaged from the first 15 ns of ten individual SMD trajectories are shown. SEM for all three

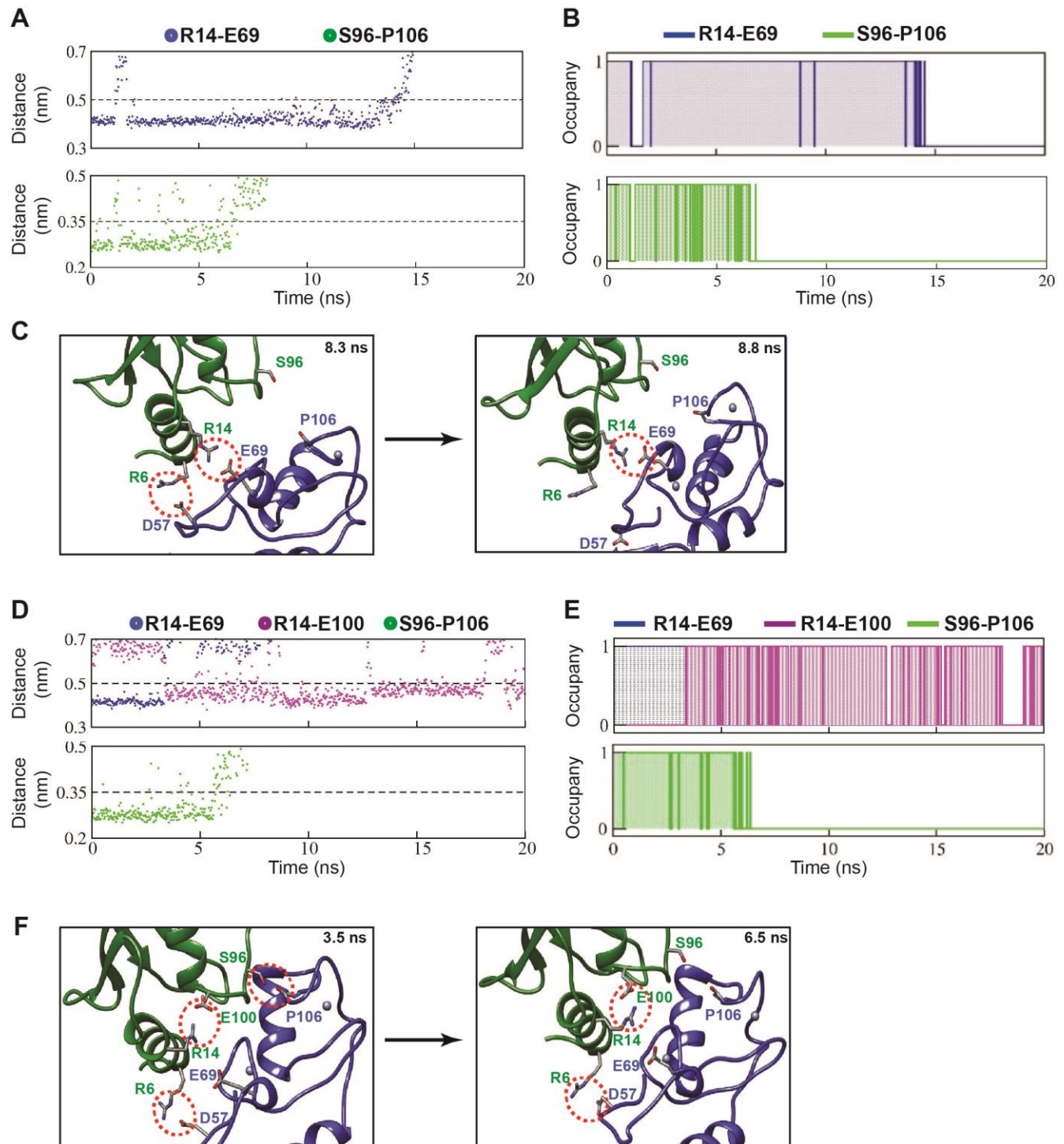332 occupancies is within 10%.

333

334
335
336 **Figure 5. Pathway of UBC13/TRAF6^{RING} complex dissociation from steered MD.**

337   A) Top: The distance between R14-Cζ and E69-Cδ atoms against time during SMD. Bottom: The

338   distance between S96-Oγ and P106-O atoms against time during SMD. B) Occupancy plots of A)

339   calculated as in Figure 2B. C) Two snapshots from the trajectory in A) are shown. S96-P106 contact

340   is disrupted at 8.3 ns followed by the R6-D57 salt-bridge break at 8.8 ns. Red dotted circles indicate

341   the polar contacts. D) Same as A) for the dUBC13/TRAF6^{RING} complex. The distance between R14-Cζ

342   and E100-Cδ atoms against time is added here. E) Occupancy plots of R14-E69 (blue), R14-E100

343   (magenta) and S96-P106 (green) contacts for the dUBC13/TRAF6^{RING} complex. F) Two snapshots

344   from trajectory analyzed in D) showed that competition between R14-E100/E69 salt-bridges as the

345   complex starts to dissociate at 6.5 ns.

346

347 **Repulsive interactions destabilize the dUBC13/TRAF6^{RING} transient complex ensemble**

348 A native protein complex forms through an intermediate species referred to as the transient/encounter

349 complex ensemble (Schreiber, Haran & Zhou 2009). These complexes are formed by native/non-

350 native long-range electrostatic interactions and have greater oriental freedom compared to the native

351 state (Tang, Iwahara & Clore 2006). Since charge distribution is altered upon deamidation, its effect

352 on the complex was estimated based on the transient complex theory (Alsallaq & Zhou 2008). The

353 method uses the native complex structure and computes association rates (k_{on}) from a basal

354 association rate constant (k_{a0}) due to random diffusion and the electrostatic interaction free energy of

355 the transient complex (ΔG_{el}). The k_{a0} values, ΔG_{el} values, and k_{on} rates computed for two complexes

356 are summarised in Table 3. The k_{on} of UBC13/TRAF6^{RING} decreased by five-fold at high salt compared

357 to low salt, confirming that electrostatic interactions are critical for the transient complex. The k_{on} of

358 dUBC13/TRAF6^{RING} reduced by three-fold compared to the wt complex at low salt. However, at high

359 salt, the drop in k_{on} was only 1.6-fold, indicating that deamidation modulates the electrostatic

360 interactions. Since the electrostatic interactions were partially screened at high salt, the effect of

361 deamidation attenuated. The position of individual atoms within each input structure remained fixed in

362 transient-complex theory calculations, and hence, the competition between salt-bridges was absent

363 during these calculations. Therefore, the changes in k_{on} upon deamidation were solely due to

364 electrostatic repulsion between E100 of UBC13 and the acidic residues on TRAF6^{RING}.

365 **Table 3. Electrostatic free energies and association rate constants (k_{a0}/k_{on}) of**
366 **UBC13/TRAF6^{RING} calculated using TransComp web server.**
367

Transient complex Ensemble	k_{a0} ($10^6 \cdot M^{-1}s^{-1}$)	10 mM NaCl		100 mM NaCl	
		ΔG_{el} (kcal mol^{-1})	k_{on} ($10^6 \cdot M^{-1}s^{-1}$)	ΔG_{el} (kcal mol^{-1})	k_{on} ($10^6 \cdot M^{-1}s^{-1}$)
UBC13/TRAF6	0.57	-2.32	28.7	-1.33	5.43
dUBC13/TRAF6	0.63	-1.59	9.36	-0.99	3.43
R14A-UBC13/TRAF6	0.62	-1.16	4.42	-0.62	1.78

368

21

369   The US simulations were analyzed to obtain molecular details of the effect of deamidation on transient

370   complexes (Figure 6). A suitable point to observe the transient complexes is the US window

371   corresponding to 3.0 nm COM separation (Figure 3B). A prominent transient interaction observed in

372   the UBC13/TRAF6^{RING} complex was between R14 in UBC13 and D57 in TRAF6, which prompted the

373   association between UBC13 and TRAF6^{RING}. Subsequently, other contacts formed to stabilize the

374   complex such that the distance between UBC13 and TRAF6^{RING} was invariant (Figure 6A-C). The CIE

375   was favorable throughout the trajectory (Figure 6D). The R14/D57 interaction was, however, unstable

376   in the case of dUBC13/TRAF6^{RING} (Figure 6C). Consequently, dUBC13 separated completely from

377   TRAF6^{RING} within 2 ns, and the CIE dropped to zero (Figure 6B-D). Interestingly, in the first 2 ns, R14

378   and E100 simultaneously interacted with D57 (Figure 6E, 6F). While the R14/D57 interaction was

379   attractive, the E100/D57 interaction was repulsive. The repulsive interaction destabilized the transient

380   complex (higher CIE in Figure 6D) and triggered its dissociation. The R14/E100 intramolecular salt-

381   bridge formed soon after dissociation, which would prevent further transient association between R14

382   and TRAF6^{RING} residues. Overall, the electrostatic repulsion between E100 and negatively charged

383   interface of TRAF6^{RING} destabilizes the dUBC13/TRAF6^{RING} transient complexes.
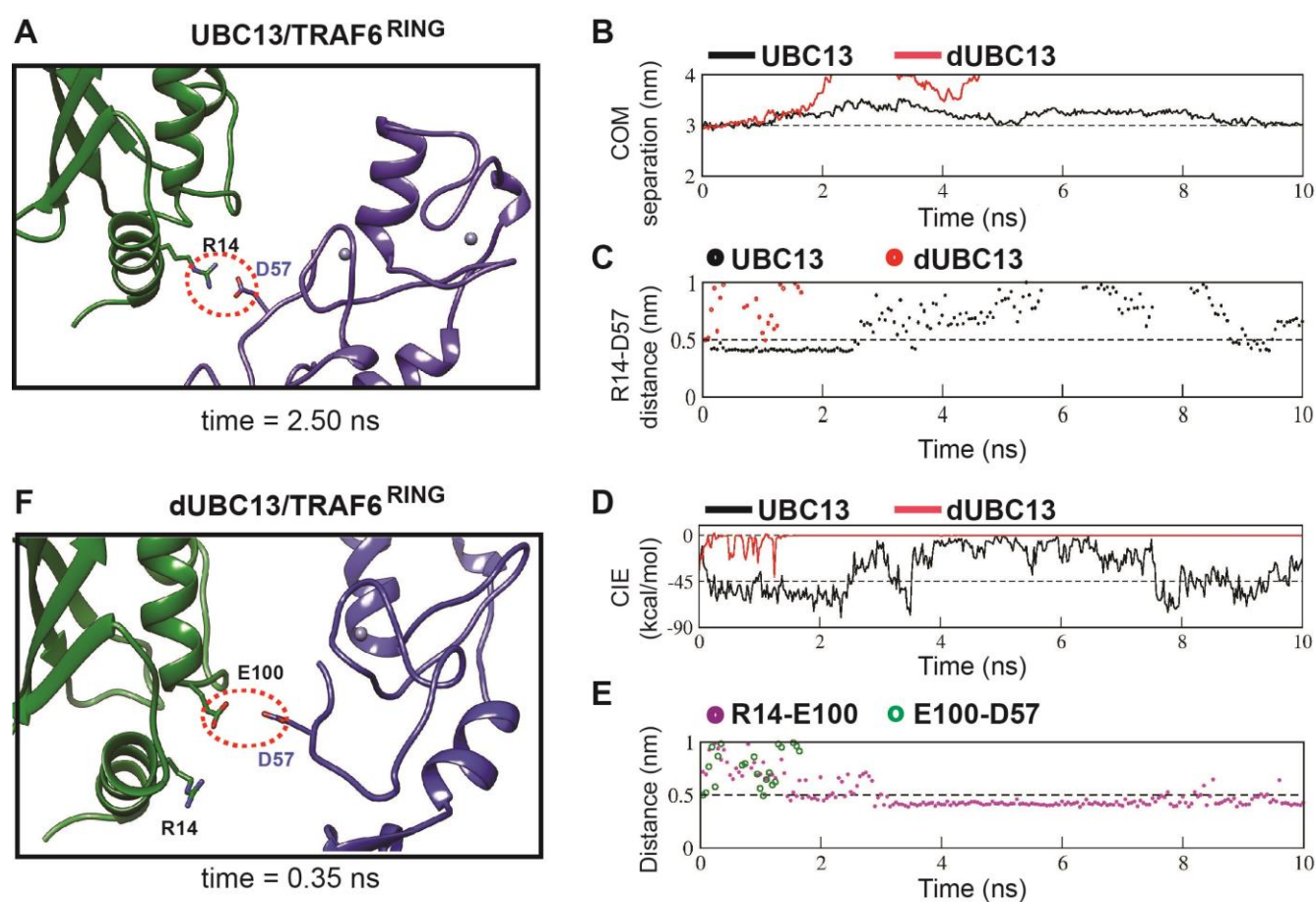
384

22

Figure 6. Analysis of transient complexes formed in the US simulations. The US window corresponding to 3 nm COM distance of separation was analyzed. (A) The transient complex of UBC13 and TRAF6^{RING} at t=2.50 ns is shown. A transient intermolecular salt-bridge between R14 and D57 is indicated by a red dotted circle. (B) The plot of COM separation against time for the UBC13/TRAF6^{RING} and dUBC13/TRAF6^{RING} complexes. (C) The distance between the R14-D57 transient contact is compared between the two complexes. The distances were measured between R14-Cζ and D57-Cγ atoms. (D) Coulombic interaction energy (CIE) plotted against time. (E) The contact distance of E100-D57 and R14-E100 contacts are shown against time for the dUBC13/TRAF6^{RING} complex. The distances were measured between R14-Cζ, E100-Cδ, and D57-Cγ atoms. (F) The transient complex of dUBC13 and TRAF6 at t=0.35 ns, where E100 contacted D57.

23

397 **Salt-bridge competition destabilizes the UBC13/TRAF6^{RING} transient complex ensemble**

398 When the transient complex theory calculations were repeated for the R14A-UBC13/TRAF6^{RING}

399 complex, the predicted k_{on} dropped significantly by six-fold at low salt (Table 3). Since repulsion due to

400 E100 is absent in R14A-UBC13, the drop in k_{on} suggests that R14-mediated interactions are crucial for

401 the transient complex. Molecular details of transient complexes observed in US simulations also

402 suggested that R14 mediated interactions favor the association of UBC13/TRAF6^{RING} complex.

403 Unbiased-association simulations were performed on the two complexes to confirm this observation.

404 From these simulations, the association probability and stability of native-like transient complexes

405 were assessed (Table 4). The mean time of association of native-like transient complexes for

406 UBC13/TRAF6^{RING} was 3-fold higher at low salt than high salt, confirming that indeed the transient

407 complex association was dependent on the long-range electrostatic interactions. However, the mean-

408 time of association in dUBC13/TRAF6^{RING} was indifferent to differences in salt-concentrations,

409 indicating that the critical transient electrostatic interactions are disrupted upon deamidation. The

410 mean time of association dropped by 2.3 fold between UBC13/TRAF6^{RING} and dUBC13/TRAF6^{RING} at

411 low salt, suggesting that deamidation affects the association of the native-like transient complex.

412 **Table 4. Summary of unbiased-association MD simulations.**

	Association Trajectories* (%)			
	10 mM NaCl (low salt)		100 mM NaCl (high salt)	
	UBC13	dUBC13	UBC13	dUBC13
Native-like association	53 (8)	20 (3)	27 (4)	33 (5)
Non-native association	47 (7)	60 (9)	40 (6)	47 (7)
No association	0 (0)	20 (3)	33 (5)	20 (3)
	Mean percentage time of native-like association (%)**			
	32 (9)	14 (9)	11 (7)	11 (5)

430 *The number of trajectories used is indicated in brackets.
431 **Standard error of mean is shown in brackets.

24

432

433   The ensemble of transient complexes observed in all the unbiased association trajectories at

434 low salt was compared between UBC13 and dUBC13 (Figure 7). The distribution of TRAF6^{RING} COMs

435 around the helix 1 of UBC13 indicates that the TRAF6^{RING} positions are tightly clustered around the

436 UBC13 interface (Figure 7A). The projections of the transient complexes on the coordinate planes

437 showed that a cluster of the transient complexes coincided with the native complex. The position of

438 TRAF6^{RING} is more dispersed when it interacts with dUBC13, and none of the clusters coincide with

439 the native complex (Figure 7B). The transient complexes were clustered by pairwise rmsd, and the

440 clusters with more than ten structures were plotted for UBC13/TRAF6^{RING} and dUBC13/TRAF6^{RING}, in

441 Figure 7C and 7D, respectively. Several clusters around R14 were absent in dUBC13/TRAF6^{RING}

442 transient complexes when compared to the wt transient complexes, indicating that the R14-mediated

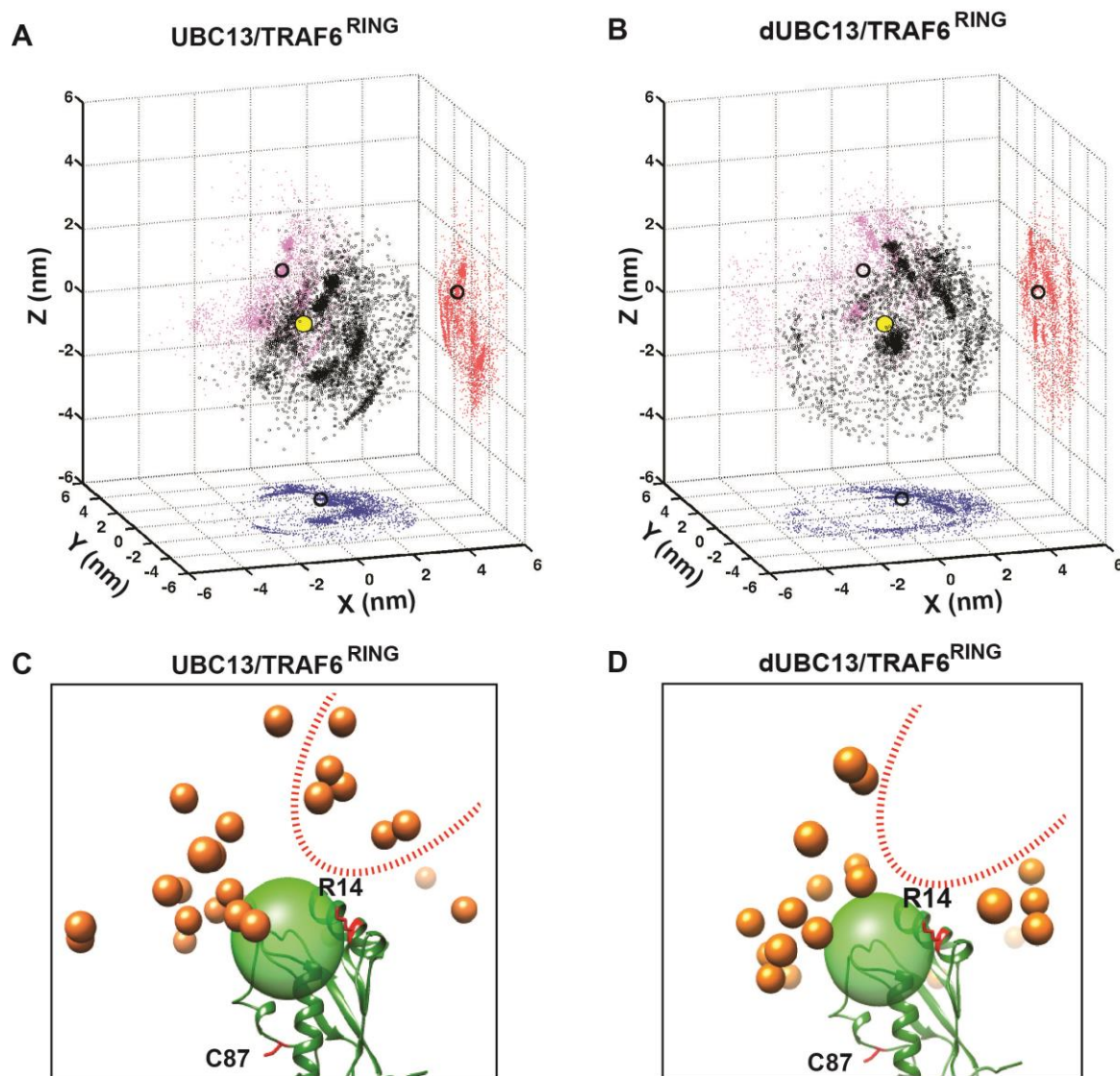443 long-range transient interactions are inhibited in dUBC13.

25

Figure 7. **Transient complexes observed during unbiased association simulations.** (A) Black open circles denote TRAF6^{RING} (aa:70-109) centers of mass around UBC13 in the Cartesian coordinate space. Red, pink and blue colored symbols denote projections of the centers of masses on the coordinate planes. Projections of the centers of mass of TRAF6^{RING} in the native complex are shown as black open circles on the coordinate planes. The center of mass of the UBC13 helix α1, which is at the center of UBC13 interface, is shown as a yellow sphere at the origin. (A) Same as in (B) for dUBC13. (C) TRAF6^{RING} clusters calculated based on pairwise RMSD between UBC13/TRAF6^{RING} complexes (cutoff = 0.45 nm) are shown as orange spheres. Only representatives for clusters with greater than ten structures are shown. The UBC13 is represented in ribbon and colored green. The center of mass of UBC13 interface is shown as a green transparent sphere with 1 nm radius. The sidechain of R14 is shown and colored red. (D) Same as (C) for dUBC13. The region

26

457 near R14, where TRAF6^{RING} clusters were absent in dUBC13 is shown as a red dotted curve in (C)

458 and (D).

459

460   The energy landscape correlating the free-energy with rmsd of TRAF6^{RING} and the minimum

461   distance between interfaces shows that multiple low-energy transient intermediates are present in the

462   UBC13/TRAF6^{RING} association pathway, which converged to the native complex (Figure S10A). In

463   contrast, a few transient intermediates are present in dUBC13/TRAF6^{RING}, and none exist in the

464   native-like conformation (Figure S10B). The association trajectories were further analyzed to detect

465   native-like complexes, whose rmsd to the native UBC13/TRAF6^{RING} structure is below 0.5 nm (Figure

466   S11A). The analysis identified one trajectory at 10 mM NaCl, where the native complex formed for 50

467   ns during the simulations (Figure 8A, S11A). In this trajectory, TRAF6^{RING} associated with UBC13

468   within the first 10 ns via the R6/D57 and R14/E69 salt-bridges (Figures 8B, Movie S4). Consequently,

469   the other relevant contacts formed, leading to the native complex at 25 ns, which persisted for the next

470   50 ns (Figure 8A, S12A). No native complex was detected in the dUBC13/TRAF6^{RING} trajectories at

471   low salt conditions (Figures S11B). At higher salt, where electrostatic interactions are partially

472   screened, a native-like complex was momentarily observed (Figures S11B, 8C, Movie S5). Herein, the

473   initial association occurred through a formation of a non-native R6/E69 salt-bridge and the S96/P106

474   hydrogen bond at ~14 ns. Soon the R14/E100 salt-bridge competed to prevent the formation of

475   R14/E69 salt-bridge, and the complex dissociated thereafter (Figures 8D and S12). In summation,

476   unbiased association simulations indicate that the competition between salt-bridges and repulsive

477   interactions perturb the ensemble of transient complexes to inhibit the association between dUBC13
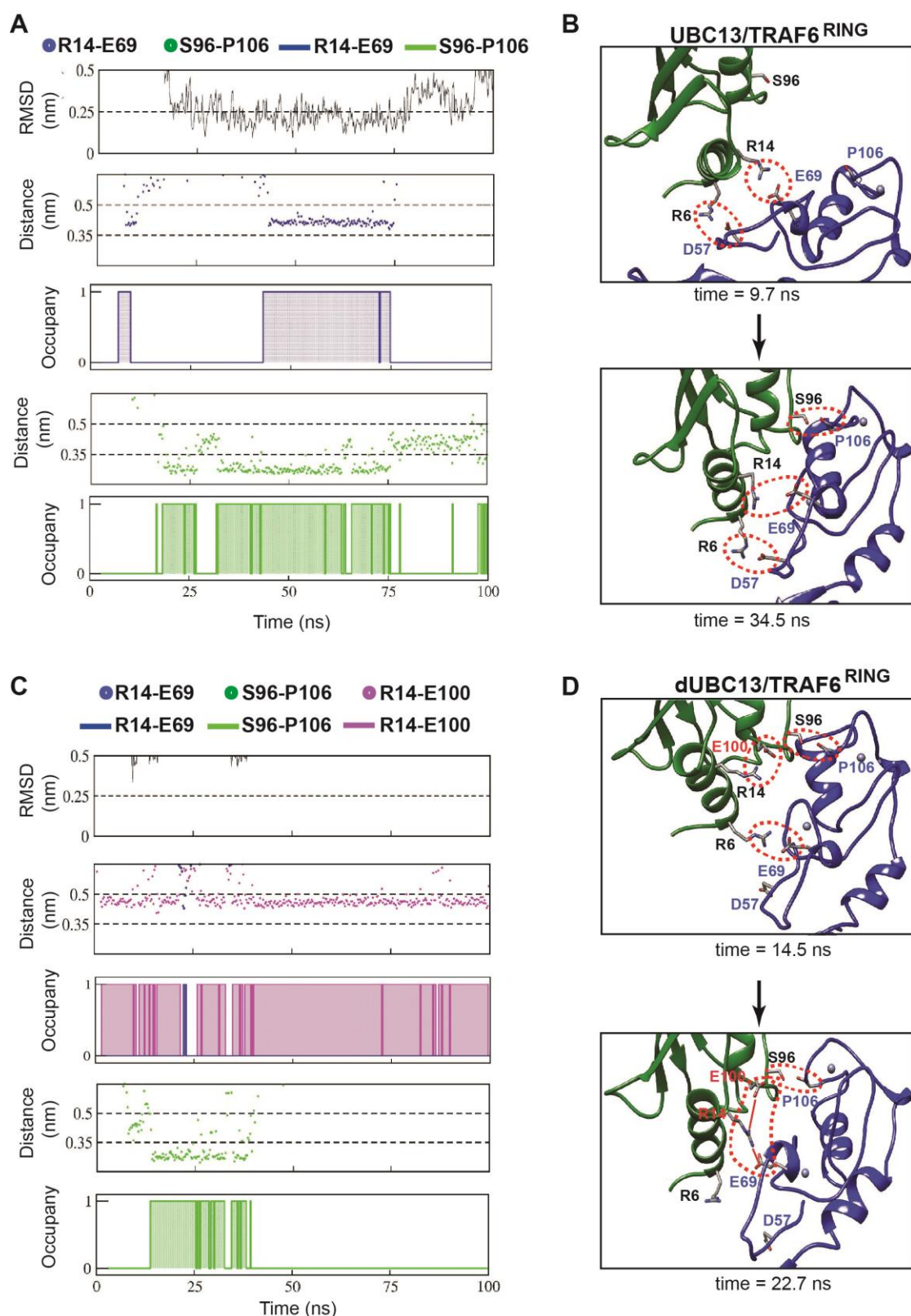
478   and TRAF6^{RING}.

479

28

Figure 8. Association pathway of the UBC13/TRAF6 complex from unbiased MD trajectory.

A) and C) shows the RMSD of TRAF6[RING], the distance between polar contacts and occupancies of

polar contacts in UBC13/TRAF6[RING] and dUBC13/TRAF6[RING] trajectory, respectively. The occupancies

are calculated as in 2B. B) Two snapshots from a trajectory in A) is shown, where the initial contacts

485   formed at 9.7 ns led to the native complex at 34.5 ns. The polar contacts at the interface are shown by

486   red dotted circles. D) Two snapshots from a trajectory in B) is shown, where the transient contacts

487   formed at 14.5 ns, but due to competition between the salt-bridges at 22.7 ns (shown by red lines), the

488   complex dissociated subsequently.

489

490 **Binding studies delineate the effects of deamidation on the UBC13/TRAF6^{RING} complex**

491 The MD simulations identified that deamidation destabilized the native complex by salt-bridge

492 competition. In addition, the transient complexes were also destabilized by salt-bridge competition and

493 repulsive interactions. NMR titrations were carried out using variants of UBC13 and TRAF6^{RING} to

494 validate the effect of each mechanism on the affinity of the complex. E69 in TRAF6^{RING} was

495 substituted to alanine to remove the acceptor of the R14/E69 intermolecular salt-bridge. The

496 substitution mimics the effect of salt-bridge competition exclusively in the native complex. When ^{15}N-

497 UBC13 was titrated with E69A-TRAF6^{RING}, the affinity dropped by 4-fold compared to the wt-complex

498 (Figure 9A). Next, R14 in UBC13 was substituted with alanine. Such a substitution mimics the effect of

499 salt-bridge competition in both the native and the transient complexes. When ^{15}N-R14A-UBC13 was

500 titrated with TRAF6^{RING}, the affinity decreased by 11-fold (Figure 9A). Assuming the effect of salt-

501 bridge competition on the transient and native complexes are mutually exclusive, the decrease in the

502 affinity of the R14A-UBC13/TRAF6^{RING} complex would be a product of these two effects. Given the

503 effect of salt-bridge competition in the native complex was 4-fold, the effect of salt-bridge competition

504 on the transient complex would be 2.8-fold (=11/4). Similarly, the repulsive effect was assumed to be

505 mutually exclusive to the salt-bridge competition. The combined effect of salt-bridge competition (both

506 on the native and transient complex) and repulsion on the binding affinity is 17-fold, whereas the effect

507 of the salt-bridge competition is 11-fold. Hence, the repulsive effect on the transient complex reduces

508 the affinity by 1.5 fold (=17/11). The reduction in binding free energy due to repulsion is 0.24 kcal mol^{-}

509 ^{1}, which compares well with the $\Delta\Delta G_{el} = \Delta G_{el}^{UBC13} - \Delta G_{el}^{dUBC13} = 0.34$ kcal mol^{-1} calculated by transient-

510 complex theory at 100 mM NaCl (Table 3). Overall, titrations studies indicated that all three events

511 have distinct effects on the binding between dUBC13 and TRAF6^{RING}.

512

513 **The effect of deamidation on transient interaction persists in the UBC13/RNF38^{RING} complex**

514   Analysis of the UBC13/RING structures shows that R14-mediated salt-bridges are common in these

515   complexes (Figure S13). An R14-mediated salt-bridge was present in four of the six complexes; CHIP,

516   LNX1, TRIM25, and ZNRF1. However, in a few complexes like UBC13/RNF4 and UBC13/RNF8, the

517   R14 mediated salt-bridge was absent. A typical RING domain from the E3 RNF38 (RNF38^{RING}, aa:

518   387-465) was chosen to study the effect of UBC13 deamidation in such cases. RNF38^{RING} can

519   activate UBC13 to synthesize polyubiquitin chains (Figure 9B). Similar to TRAF6, the RNF38^{RING} fails

520   to activate dUBC13 (Figure 9B). In silico modeling of the UBC13/RNF38^{RING} native complex suggests

521   that like RNF4 and RNF8, RNF38^{RING} lacks a negatively charged residue at the position corresponding

522   to E69 in TRAF6^{RING} (replaced by L412, Figure S14). There are no negatively charged residues at the

523   interface that can be an acceptor of the salt-bridge (Figure S14B). However, there are several acidic

524   residues at the vicinity, similar to TRAF6^{RING}, which can form non-native transient interactions with

525   UBC13 (Figure S14C, S14D). In the absence of the intermolecular salt-bridge in the native complex,

526   the loss of catalytic activity upon deamidation implies a drop in the UBC13/RNF38^{RING} affinity induced

527   solely by perturbation of the transient complexes.

528   NMR titrations measured the effect of deamidation on the interaction between UBC13 and

529   RNF38^{RING}. When RNF38^{RING} domain was titrated into a sample of ^{15}N-UBC13 (Figure 9C), major

530   CSPs were observed in the α1-helix, β3-β4 loop, and the loop between α$_{3-10}$ and α1-helix (Figures 9D

531   and 9E). Unlike the UBC13/TRAF6^{RING} interface, the hydrophobic β3-β4 loop has a significant number

532   of CSPs at the UBC13/RNF38^{RING} interface. Consequently, the K_d value of UBC13/RNF38^{RING}

533   interaction was lower 0.04 (±0.01) mM (Figure 9I). Considerable peaks shifts were also detected when

534   RNF38^{RING} was titrated to a sample of ^{15}N-dUBC13 (Figure 9F). However, the CSPs in dUBC13 were

535   reduced compared to UBC13 at the same protein: ligand stoichiometry, indicating reduced affinity

536   (Figures 9F-H). Fitting of peak shifts against ligand: protein ratio yielded the K_d to be 0.25 (±0.08) mM,

537   which corresponds to a 6-fold drop in affinity.

538   Both the effects of salt-bridge competition and repulsive interactions on transient complex

539   could be at play in the dUBC13/RNF38^{RING} complex. The titration was repeated with R14A-UBC13,

32

540   which mimics the salt-bridge competition in the transient complex. The K_d of R14A-UBC13/RNF38^{RING}

541   interaction was 0.10 (±0.03) mM, corresponding to a 2.5-fold decrease in affinity exclusively due to the

542   salt-bridge competition. Overall, the effect of deamidation on perturbing the ensemble of transient

543   complexes could be verified in another RING domain, which indicated that the mechanism could be

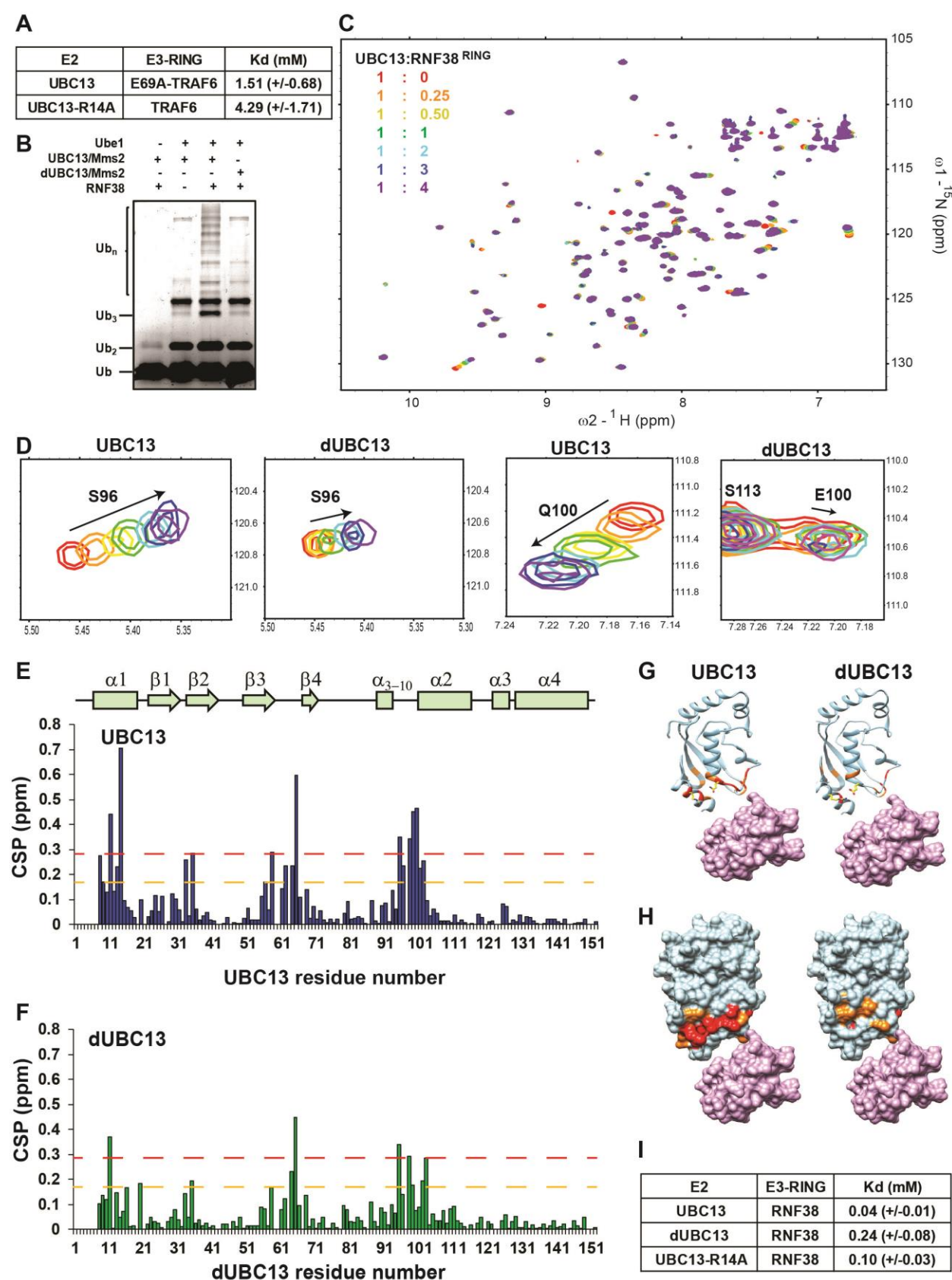544   ubiquitous in UBC13/RING complexes.

545

Figure 9. Activity and interactions of the UBC13/RNF38^RING complex. A) The measured

dissociation constants of mutants of UBC13/TRAF6^RING complex are given as Mean+/-SD. B) *In vitro*

548   ubiquitination assay was performed using Ube1, UBC13/Mms2 (or dUBC13/Mms2) and RNF38. C)

549   Overlay of the ^{15}N-edited HSQC spectra of free UBC13 (red) with different stoichiometric ratios of

550   RNF38^{RING} as given in the top left-hand side of the spectra. D) Regions of the HSQC spectra are

551   expanded to show the UBC13 and dUBC13 peaks during titration with RNF38^{RING}. E) The CSPs for

552   each residue in UBC13 upon binding to RNF38^{RING}. The orange and red dashed lines correspond to

553   Mean+SD and Mean+2*SD, respectively. The secondary structure alignment of UBC13 against its

554   sequence is provided above the plot. F) The CSPs for each residue in dUBC13 upon binding to

555   RNF38^{RING}. The dashed lines are replicated from E). Significant CSPs were mapped on the UBC13

556   and dUBC13 structure using both the G) ribbon and H) surface representation. The UBC13 and

557   dUBC13 are colored in light blue. The residues with CSPs above Mean+SD and Mean+2*SD are

558   colored in orange and red, respectively. The RNF38^{RING} domain is surface rendered and colored in

559   magenta. I) The measured dissociation constants of UBC13 and its mutants with RNF38^{RING} domain

560   are given as Mean+/-SD.

561

RING domains fail to bind and activate the dUBC13~Ub conjugate

If the RING domains bind weakly to dUBC13, their ability to activate the dUBC13~Ub conjugate should be compromised, which was tested by binding and activity assays. First, the conjugation of donor Ub to the UBC13 and dUBC13 were compared by an *in-vitro* conjugation reaction, where the E2s were incubated with E1, K63A-Ub, and ATP for 15 min. Both the UBC13 and dUBC13 conjugated with the donor Ub with similar efficiency, indicating that deamidation does not hamper the step of E2~Ub conjugation by E1 (Figure 10A and Figure S16). In the UBC13~Ub/TRAF6^{RZ3} complex, the RING domain and ZF1 domain makes additional contacts with donor Ub to stabilize the complex further. These contacts could rescue the loss in affinity between UBC13 and RING domain upon deamidation. Hence, the binding of UBC13~Ub and dUBC13~Ub to TRAF6^{RZ3} was compared. MBP-Mms2 was incubated with UBC13~Ub conjugate and TRAF6-RZ3 on amylose beads, washed thoroughly, separated on the gel and imaged. While UBC13~Ub conjugate bound to TRAF6^{RZ3}, dUBC13~Ub conjugate failed to do so (Figure 10B and Figure S16). In a similar experiment, GST-RNF38^{RING} and UBC13~Ub were incubated on GST-beads, washed and separated on a gel. UBC13~Ub but not dUBC13~Ub bound to RNF38^{RING} (Figure 10C). Altogether, the binding experiments confirmed that secondary interactions between Ub/RING or Ub/ZF1 could not compensate for the loss of primary interaction between UBC13 and RING.

The activation of UBC13~Ub conjugates by the RING domains were measured by the kinetics of single-round Ub discharge from the UBC13~Ub. UBC13 (or dUBC13) was first conjugated with K63A-Ub. Then the conjugation reaction was quenched, followed by the addition of Mms2, RING domains, and free Lysine. TRAF6^{RING} could effectively discharge Ub from UBC13~Ub, but not from dUBC13~Ub (Figure 10D, G, H). Similarly, RNF38^{RING} could discharge Ub from UBC13~Ub but not from dUBC13~Ub (Figure 10E, I, J). When the concentration of the RNF38^{RING} was increased by five-fold to compensate for the reduced affinity of dUBC13~Ub/RNF38^{RING} complex, the rate of Ub discharge improved by six-fold, which confirmed that the inefficient discharge is due to the reduced affinity of dUBC13~Ub/RNF38^{RING} complex (Figure 10K and 10F).

36

588   The lysine of the acceptor Ub at the growing end of a poly-Ub chain (either unanchored or

589   anchored on a substrate), attacks the E2~Ub active site to transfer the donor Ub. The kinetics of

590   single-round di-Ubiquitin (Ub_2) synthesis was monitored to investigate if the deamidation of UBC13

591   affects the activity of UBC13 and its interaction with acceptor lysine at the active site. Here the lysine

592   of the acceptor Ub mimics the acceptor lysine of growing poly-Ub chain. UBC13 (or dUBC13) was

593   conjugated with donor K63A-Ub. Then Mms2, RNF38^{RING} and acceptor D77-Ub was added in the

594   reaction mix, which was then monitored over time to detect the synthesis of Ub_2. The rate of Ub_2

595   synthesis was rapid for UBC13 but slow for dUBC13 (Figure 10L). Kinetic analysis indicated that the

596   reaction rate for the dUBC13/RING complex is similar to the rate of UBC13 in the absence of RING

597   (Figure 10M and Figure S17), indicating that the catalytic effect of RING is absent in the

598   dUBC13/RING complex. A comparison of the kinetic parameters between UBC13 and dUBC13

599   indicated that deamidation does not significantly affect the Km of the substrate, but drastically affects

600   the Kcat of the reaction (Figure 10N and Figure S17). This confirms that the area around the active

601   site is not perturbed by deamidation, as was observed by NMR in Figure S2. Furthermore, in the

602   absence of a RING domain, the Kcat of UBC13 and dUBC13 is similar, confirming that the catalytic

603   activity of UBC13 is unaffected upon deamidation, similar to the observation of Figure 1C. However,

604   unlike UBC13, the Kcat of dUBC13 does not increase in the presence of RING, confirming that RING

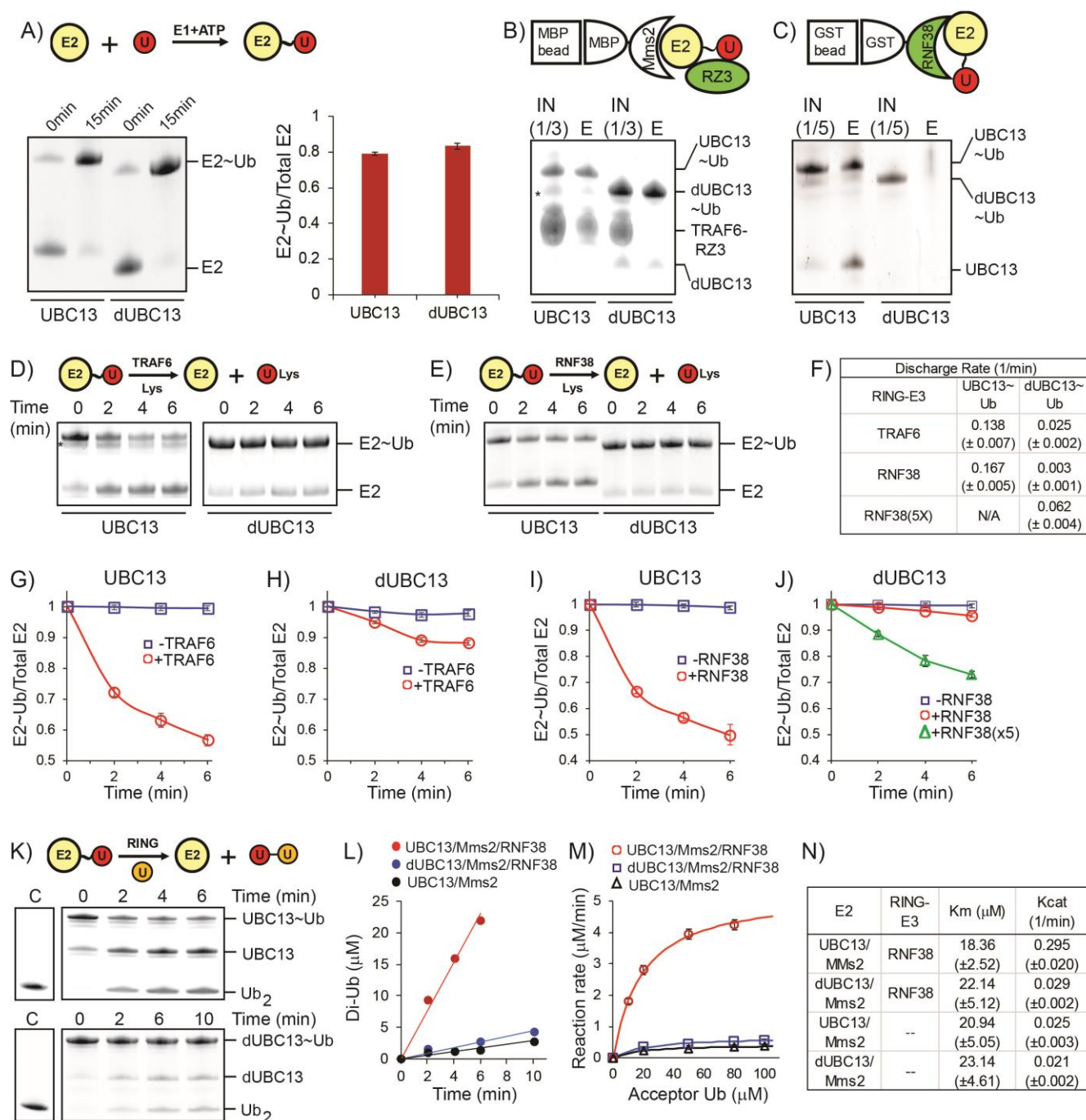605   domains fail to bind and activate the dUBC13~Ub conjugate.

606

607

Figure 10. Activation of UBC13~Ub conjugates by RING domains. A) A comparison of Ub
conjugation to UBC13 and dUBC13. E1, ATP, and UBC13/dUBC13 were incubated in reaction buffer
for 15 min, quenched by adding EDTA and separated on SDS page. The amount of E2~Ub
conjugates were quantified and plotted in the right section. The values are the mean of three
reactions, and the error is the standard deviation of the same. B) Affinity pull-down experiment was
performed by incubating MBP beads with MBP-Mms2, UBC13~Ub (or dUBC13~Ub) and TRAF6[RZ3],
washed thoroughly and separated on SDS gels. The asterisk denotes impurities. C) Affinity pull-down

38

615   experiment was performed by incubating GST beads with GST-RNF38^{RING} and UBC13~Ub (or

616   dUBC13~Ub), washed thoroughly and separated on SDS gels. D) Single-round discharge of Ub from

617   UBC13~Ub and dUBC13~Ub catalyzed by TRAF6^{RING} was monitored. UBC13 was conjugated with

618   Ub, and the reaction was quenched. Then Mms2, TRAF6^{RING,} and Lysine were added to the reaction

619   mixture, and E2~Ub and free E2 was monitored over time. The proteins bands in D) were quantified

620   and plotted in G) and H). E) Same as in D), where the discharge is catalyzed by RNF38^{RING} domain.

621   The proteins in E) are quantified and plotted in I) and J). The rate of discharge in each case was

622   calculated as discharge-rate= (Total E2-E2~Ub)/(Total E2.time) for the initial time points and given in

623   F). K) The rate of Ub$_2$ synthesis was monitored over time. UBC13 or dUBC13 was conjugated with Ub,

624   and the reaction was quenched. Then Mms2, RNF38^{RING} and Acceptor Ub was added to the reaction

625   mixture, and the synthesis of Ub$_2$ was monitored over time. L) The rate of Ub$_2$ synthesis for UBC13

626   and dUBC13 are compared at substrate (acceptor-Ub) concentration of 50 μM. M) The reaction rates

627   for UBC13 and dUBC13 are compared at various substrate concentrations. N) The kinetic parameters

628   of Ub$_2$ synthesis for UBC13 and dUBC13 are given in a table. The Ub used in all the experiments of

629   this figure is K63A-Ub, except the acceptor Ub used in K)-M) is D77-Ub.

630

631 **Discussion**

632 Protein deamidation can have significant functional consequences for innate immune signaling (Zhao

633 et al. 2016), which justifies its emergence as a powerful tool employed by pathogenic bacteria to

634 suppress the immune response (Washington, Banfield & Dangl 2013). However, little is known about

635 the molecular mechanism underlying deactivation of immune signaling by deamidation. The *Shigella*

636 *flexineri* effector OspI suppresses the inflammatory response (NF-κB pathway) via deamidation of

637 UBC13 at Q100. By an unknown mechanism, deamidation of Q100 to E100 inhibits the synthesis of

638 K63-linked polyubiquitin chains by the UBC13/TRAF6 complex, preventing the downstream activation

639 of NF-κB pathway. Q100 is present at the vicinity of UBC13/TRAF6 interface but does not form direct

640 contact with TRAF6. We report that deamidation neither alters the fold nor the enzymatic activity of

641 UBC13. NMR and kinetics studies indicate that deamidation does not alter the active site and the Km

642 of acceptor lysine. Instead, it inhibits the interaction between UBC13 and RING domains to diminish

643 the catalytic effect of the RING. The dUBC13/TRAF6 interaction is inhibited because deamidated

644 E100 competes with an intermolecular R14/E69 salt-bridge at the UBC13/TRAF6^{RING} interface to form

645 an intramolecular salt-bridge, which destabilizes the native complex. The new intramolecular salt-

646 bridge also inhibits the long-range transient interactions formed by R14 with TRAF6^{RING}. In addition,

647 repulsive interactions between E100 and the negatively charged interface of TRAF6^{RING} destabilize the

648 transient complexes. Cumulatively, these mechanisms reduced the affinity between UBC13 and

649 TRAF6^{RING} by 17-fold. Consequently, its efficiency in activating the UBC13~Ub conjugate drops by 6-

650 fold (Figure 10F). The effect of deamidation is also manifested in another UBC13/RING complex.

651 Deamidation reduced the rate of Ub-discharge and the rate of Ub_2 synthesis by several folds in the

652 UBC13/RNF38^{RING} complex (Figure 10F and 10N). These results provide first insights into the

653 molecular mechanism behind the inactivation of the Ubiquitin pathway by bacterial deamidation.

654   For several E3s like RNF38, the RING domain can function as a monomer (Buetow et al. 2015).

655 For others like TRAF6, the RING domains function as dimers (Middleton et al. 2017a; Yin et al. 2009).

656 Since deamidation perturbed the binding of UBC13 to both TRAF6 and RNF38, it is likely that

40

657 deamidation inactivates UBC13 for both homo/hetero-dimeric RING-E3s. In dimeric RINGs like

658 TRAF6, the proximal RING interacts with one unit of UBC13~Ub, and the distal RING interacts with

659 the donor Ub of another UBC13~Ub (Figure S15). Additionally for TRAF6 dimer, the first zinc-finger

660 following the RING domain of one protomer also interacts with the donor Ub of the UBC13~Ub bound

661 to another protomer (Middleton et al. 2017b). However, the binding between UBC13 and TRAF6^{RING} is

662 independent of dimerization (Yin et al. 2009), indicating that binding between UBC13 and proximal

663 RING is primary for the rest of the contacts. Indeed, deamidation inhibited the binding of UBC13 to

664 both TRAF6^{RING} and to the longer dimeric TRAF6^{RZ3}, confirming that secondary interactions between

665 Ub/RING or Ub/zinc-finger cannot compensate for the loss of primary E2/RING interaction.

666 Though the interface of a protein complex has numerous interacting residues, a few hotspot

667 residues contribute significantly to the binding energy than the rest (Moreira, Fernandes & Ramos

668 2007). Hotspot prediction algorithms reported R14 to be a hotspot at the UBC13/TRAF6^{RING} interface

669 (Meireles n.d.; Zhu & Mitchell 2011). Analysis of all the UBC13/RING (or U-box) structures shows that

670 intermolecular salt-bridges involving R14 are present in several of the UBC13/RING complexes

671 (Figure S13). Binding studies by isothermal titration calorimetry measured that R14A substitution

672 reduced the binding energy of UBC13/ZNRF1^{RING} complex by ~1.2 kcal mol^{-1} (Behera et al. 2018).

673 Similarly, our NMR titrations measured that R14A substitution reduced the binding energy by ~1.4 kcal

674 mol^{-1} in the UBC13/TRAF6^{RING} complex. Altogether, R14 appears to be a hotspot at the

675 UBC13/TRAF6^{RING} interface. Deamidation of UBC13 disrupts the salt-bridge between R14 and E69

676 due to competition from E100, which destabilizes the UBC13/TRAF6^{RING} complex. Recently, the salt-

677 bridge competition or "theft" mechanism was observed in the binding switch of Raf Kinase Inhibitory

678 Protein (RKIP) to either Raf-1 or GPCR-kinase 2 (Skinner et al. 2017). Phosphorylation of S153 in

679 RKIP created a new salt-bridge between pS153 and K157, which disrupted the pre-existing salt-

680 bridges involving K157 and resulted in the local unfolding of RKIP. The unfolding inhibited binding of

681 RKIP to Raf-1 but promoted its binding to GPCR-kinase 2. Unlike RKIP, deamidation does not alter

682 the local fold of UBC13. While intramolecular salt-bridges compete within RKIP, the competition is

41

683 between an intramolecular and intermolecular salt-bridge in UBC13. As expected, the intramolecular

684 salt-bridge is dominant and effectively outcompetes the intermolecular salt-bridge (Figure 5E).

685 Besides the hotspots, electrostatic substitutions at the vicinity of the interface can also increase

686 protein-protein association (and affinity) by several folds (Selzer, Albeck & Schreiber 2000). Such

687 substitutions would shift the equilibrium between native and transient associations (Volkov et al.

688 2010). The proper conformation of transient complexes is vital for two proteins to form a stable,

689 productive complex (Pan et al. 2019; Schilder & Ubbink 2013). How PTMs affect native protein-protein

690 interactions observed in the ground state structure of the complex is well appreciated. However, little

691 is known about how PTMs can affect the higher energy transient protein-protein associations. PTMs

692 like phosphorylation, eliminylation, and deamidation can change the surface electrostatics of a protein

693 (Ribet & Cossart 2010) to modulate the conformation and population of transient complexes

694 significantly. By a combination of all-atom simulations and experimental data, this study provides

695 molecular details of how PTMs can modulate transient protein-protein associations to inhibit

696 interaction. In the dUBC13/RNF38 complex, deamidation only alters transient associations.

697 Nonetheless, this causes a 10-fold drop in the catalytic activity of the complex (Figure 10N), indicating

698 that modifying the transient protein-protein associations can severely affect function.

699 The fate of the polyubiquitinated substrate depends on the linkage specificity of the conjugated

700 polyubiquitin chain, which in turn depends on the specificity of the E2/E3 interaction. Rationally

701 designed E2/E3 interactions can change the fate and function of cellular proteins (van Wijk et al.

702 2009). Hence, the interfacial contacts that determine E2/E3 specificities are a subject of intense

703 research (Christensen, Brzovic & Klevit 2007; Soss et al. 2011; van Wijk et al. 2009, 2012). The

704 strength and functionality of E2/E3 interactions have been typically tested by mutating the interfacial

705 residues (Christensen, Brzovic & Klevit 2007; Das et al. 2009, 2013). This work provides evidence that

706 transient interactions have an equally significant role in E2/E3 interaction and function. Rational design

707 strategies will improve significantly by incorporating transient E2/E3 interactions.

708   In several cases, the native interactions cannot explain the functional implications of PTMs.

709 This study introduces a new approach to understand the functional role of PTMs by considering their

710 transient interactions. For example, spontaneous deamidation (non-enzymatic) is rampant in age-

711 onset diseases, including neurodegenerative and ocular diseases. Deamidation of amylin accelerates

712 its aggregation and amyloid formation (Dunkelberger et al. 2012). Crystallins deamidate with age,

713 which promotes its aggregation to trigger cataract (Pande, Mokhor & Pande 2015). Crystallin surfaces

714 are highly charged, and possibly deamidation alters their charge distribution to promote non-native

715 associations leading to aggregation. However, the sites of deamidation on crystallins do not provide a

716 clear mechanism of the process. Deamidation-induced modulation of transient protein-protein

717 associations may explain the tendency of these proteins to aggregate.

718   The bacterial effector OspI from *S. flexineri* presents a fascinating case, wherein a pathogen

719 employs subtle mechanisms like salt-bridge competition and modification of the transient protein-

720 protein associations, to produce a remarkable cumulative effect of inhibiting protein-protein interaction,

721 polyubiquitination, and the host immune response. Such a mechanism could be a ubiquitous mode of

722 regulating cellular pathways by PTMs.

723

724 **Acknowledgments**

730

731 **Methods**

43

Initial structures and molecular modeling

The interfacial contacts of UBC13/TRAF6^{RING} were obtained from PDB entry 3HCU using the typical cut-offs in the contact analysis tool in UCSF Chimera (Pettersen et al. 2004). Initial structures of UBC13 and TRAF6^{RING} for MD simulations and association rate constant (k_{on}) estimation were obtained from the PDB entry 3HCU (Chain A/B), which represents a model of the native complex. For MD simulations of TRAF6^{RING}, a C-terminal truncated model comprising of residues 50-148 was used. Substitutions were introduced by replacing existing sidechain with the best aligning rotamer from the Dunbrack rotamer library (Dunbrack 2002) in UCSF Chimera (Pettersen et al. 2004). Electrostatic surface potentials of UBC13 and TRAF6^{RING} were calculated using the Adaptive Poisson-Boltzmann Solver (Baker et al. 2001). The in silico model of UBC13/RNF38^{RING} was generated by superposing RNF38^{RING} (PDB entry 4V3K, chain F) onto TRAF6^{RING} in the UBC13/ TRAF6^{RING} complex using the structural alignment tool in UCSF Chimera. The calculations based on transient-complex theory were performed using the TransComp webserver (Qin, Pang & Zhou 2011).

General molecular dynamics (MD) simulation protocol

All simulation methodologies employed in the study were performed using the AMBER99SB-ILDN force field ((Best & Hummer 2009; Hornak et al. 2006; Lindorff-Larsen et al. 2010). Unbiased MD simulations were performed in GROMACS version 4.6.4, while biased simulations were performed using the pulled code in Gromacs 5.1.2 (Abraham et al. 2015; Hess et al. 2008). All the acidic and basic residues apart from Histidines were modeled in their charged states. The Zinc AMBER force field (Peters et al. 2010) parameters were used to model the two zinc coordination sites within the TRAF6^{RING} domain. The initial structures were solvated in an appropriate box using the TIP3P (Jorgensen et al. 1983) water model. The non-bonded ion parameters proposed by Joung and Cheatham (Joung & Cheatham 2008) were used to model Na$^+$ and Cl$^-$ ions in TIP3P water. Additional non-bonded parameter corrections proposed by Yoo and Aksementiev for cation-chloride (Yoo & Aksimentiev 2012), amine-carboxylate (Yoo and Aksimentiev, 2015) and aliphatic carbon-carbon (Yoo & Aksimentiev 2016b) interactions were used for all simulations to eliminate overestimation of the

44

759 strength of these interactions. A suitable number of counterions were added to neutralize the residual

760 charge of the system, and additional ions were added to the box depending on the desired

761 concentration. The electrically neutral, solvated system was then subjected to energy minimization

762 using the steepest descent method for a maximum of 5000 steps until the maximum force on any

763 atom was less than 1000 kJ mol^{-1} nm^{-1}. Production simulations were performed under periodic

764 boundary conditions at a temperature of 300 K, and 1 bar pressure (NPT ensemble) following

765 equilibration carried out for 600 ps with 2 fs time steps. Temperature control was achieved using the v-

766 rescaling thermostat (Bussi, Donadio & Parrinello 2007) for both equilibration (T_c = 0.1 ps) and

767 production (T_c = 2.5 ps) steps. The Berendsen (Berendsen et al. 1984) (T_p = 1 ps) and Parrinello-

768 Rahman (Parrinello & Rahman 1981) barostat (T_p = 5 ps) were employed for pressure control during

769 equilibration and production steps respectively. All bond lengths were constrained using the LINCS

770 (Hess 2008) algorithm. Virtual interaction sites were employed for hydrogen atoms (Bjelkmar et al.

771 2010), which permitted the use of a 5 fs time step. Short-range electrostatics and van der Waals

772 interactions were calculated using a 1.0 nm cut-off. Long-range electrostatics were calculated using

773 the smooth Particle Mesh Ewald (PME) method (Darden, York & Pedersen 1993; Essmann et al.

774 1995). An analytical dispersion correction was applied to approximate the effect of long-range van der

775 Waals interactions.

776

777 **Analysis of conventional MD simulations**

778 Simulations of free dUBC13 and UBC13/dUBC13 native complexes with TRAF6^{RING} were performed

779 using general MD protocol described above. Salt-bridge occupancies were computed using a cut-off

780 distance of 0.5 nm between arginine Cζ and glutamate Cδ atoms using a python script. For unbiased-

781 association simulations, UBC13/dUBC13 and TRAF6^{RING} were separated along with the x component

782 of the vector connecting their center of masses by 4 nm in a cubic box with an edge length of 12.6 nm.

783 This results in a box volume equal to ~2000 nm^3 and the resulting concentration of each protein

784 species equal to ~1 mM. Fifteen independent association runs (100 ns each with different initial atomic

785 velocities) were performed at 10 mM NaCl and 100 mM NaCl concentrations.

45

786   Trajectories were analyzed every 250 ps using analysis scripts available within the Gromacs

787   package. Minimum distances were measured between UBC13 and TRAF6^{RING} to identify native-like,

788   non-native, and non-associating trajectories using g_mindist. Native-like transient complex formation

789   was considered to occur in a trajectory when the minimum distance between the sidechain nitrogen

790   atoms of R6/K10/R14 (UBC13) and sidechain oxygen atoms of D57/E69 (TRAF6^{RING}) fell below 0.35

791   nm and persisted for more than 8 ns. Among the remaining trajectories, minimum distances were

792   measured between all UBC13 and TRAF6^{RING} heavy atoms. Non-native and non-associating

793   trajectories were then identified using the same distance and persistence period cut-off.

794   The spatial distribution of TRAF6^{RING} COMs around UBC13/dUBC13 was obtained by calculating

795   the displacement between COMs of Cα atoms of helix-I in UBC13 and TRAF6^{RING} (70-109) using

796   g_dist and plotted for all fifteen association trajectories. RMSD-based structural clustering (Daura et

797   al. 1999) with a cut-off of 0.45 nm was performed on pairwise rmsd matrices (determined using

798   g_rmsd) of the combined trajectories (1.5 μs) using UBC13/dUBC13 (Cα atoms) as a reference for

799   superposition to obtain the UBC13/TRAF6^{RING} transient complex clusters. The rmsd was computed for

800   the backbone atoms of both UBC13 and TRAF6^{RING} between all trajectory snapshots. The output

801   structures of the complex were then superposed on UBC13 (PDB: 3HCU) to obtain the location of

802   TRAF6^{RING} cluster representatives. Native complex formation was identified by measuring the Cα rmsd

803   of TRAF6^{RING} with respect to its position in the crystal complex for trajectories which exhibited the

804   formation of native-like transient complexes using UBC13 (Cα atoms) as a reference for superposition.

805   Two-dimensional free energy landscapes for UBC13/dUBC13 association with TRAF6^{RING} were

806   computed as a function of minimum distance (for salt-bridges between UBC13-R6/K10/R14 and

807   TRAF6-D57/E69) and TRAF6^{RING} rmsd using a python script. Bin width of 0.02 nm was used for both

808   coordinates, and the free energy (ΔG) corresponding to each bin were determined using the relation:

809     $$\Delta G\ (R1,\ R2)\ =\ -\ k_B T\ [\ ln\ P_i - ln\ P_{max}\ ] \qquad\qquad (1)$$

810   where R1/R2 are the two reaction coordinates, k_B is the Boltzmann constant, T is the temperature, P_i

811   is the joint probability of R1/R2 in a given bin and P_{max} is the max value of the probability. The lowest

46

812 free energy state corresponds to ΔG = 0. Visualization of MD trajectories and analysis of the native

813 contacts was performed using the MD analysis tool in UCSF Chimera.

814

815 **Umbrella sampling (US)**

816 This is an enhanced-sampling method (Torrie & Valleau 1977) to determine free energy differences for

817 state transformations by calculating the potential of mean force (PMF) as the function of a predefined

818 reaction coordinate (ξ). This amounts to performing multiple, equilibrium MD simulations along with a

819 range of ξ values and determining the corresponding free energy ($A(\xi)$). At points along ξ which are

820 referred to as windows, a harmonic restraining potential (w_i) is added to the original Hamiltonian in

821 order to restrain the system close to a target value (ξ_i):

$$E^b(r) = E^u(r) + w_i(\xi) \qquad (2)$$

$$w_i(\xi) = k/2 * (\xi - \xi_i)^2 \qquad (3)$$

824 In equation (2), $E(r)$ denotes the potential energy function (force field) of the system as a function of

825 atomic coordinates (r). Subscripts b and u indicate biased and unbiased energies. *k is* the force

826 constant for the harmonic bias potential whose magnitude determines the range of ξ values sampled

827 within each window. The application of the bias potential particularly improves sampling in high energy

828 regions along ξ which are poorly sampled in conventional MD simulations. The modified energy

829 function yields biased probability distributions ($P_i^b(\xi)$) of ξ from which the unbiased, free energy ($A_i(\xi)$)

830 of a window can be computed using the relation:

$$A_i(\xi) = -k_B T ln P_i^b(\xi) - w_i(\xi) + F_i \qquad (4)$$

832 The value of F_i needs to be determined for all windows to combine adjacent windows and obtain

833 the global free energy profile ($A(\xi)$), which describes state transformation. The weighted histogram

834 analysis method (WHAM) (Kumar et al. 1992) is widely used to determine optimal values of F_i in an

835 iterative fashion so as to obtain convergence of the free energy profile.

836 Similar to previous studies which utilized the US approach to study the energetics of protein-

837 protein association, the center of mass (COM) separation along the x-axis was chosen as the reaction

838 coordinate to calculate the PMF for Barnase/Barstar and UBC13/TRAF6 [RING] association. Barstar and

47

839 UBC13 were translated along the x-axis of the vector joining the COM between their binding partners

840 to positions separated by 0.1 nm intervals to achieve final separations of 4.0 and 4.5 nm respectively.

841 Each window was simulated in a rectangular box of dimensions 12.6 nm x 9.0 nm x 9.0 mm following

842 equilibration. During production MD (10 ns for each window), a harmonic restraining potential (k =

843 1500 kJ mol^{-1} nm^{-2}) was applied to the COM vector in each window and data were collected every 250

844 fs. The biased COM probability distributions from each window were analyzed based on WHAM and

845 combined to obtain the global free energy (PMF) profile using the g_wham analysis tool (Hub, De

846 Groot & Van Der Spoel 2010). A total of 200 bins were used to construct a mean PMF profile from five

847 independent time blocks (1.5 ns each from 2.5 to 10 ns) for each window (Table S1). A tolerance of

848 10^{-9} was used to check for convergence. The free energy of association (ΔG_{PMF}) along the COM

849 coordinate was determined by setting the free energy profile to zero in the unbound state (4.0 nm for

850 Barnase/Barstar and 4.5 nm for UBC13/TRAF6^{RING}) and determining the value of the profile at mean

851 COM separation in the native complex (2.3 nm for Barnase/Barstar and 2.7 nm for UBC13/TRAF6^{RING})

852 window during production MD.

853

854 **Steered MD**

855 This is a non-equilibrium, enhanced-sampling technique wherein a time-dependent biasing potential

856 is applied on a selected atom/COM of atomic groups to induce perturbation in the system (Grubm ller,

857 Heymann & Tavan 1996). This is achieved by means of a moving dummy atom attached to the pull

858 group via a stiff harmonic spring. This method has been previously employed to study the unfolding of

859 protein domains and the dissociation of protein-ligand complexes. In this study, we carried out force-

860 induced unbinding of TRAF6^{RING} from UBC13 using the constant velocity pulling method along the x-

861 axis to a COM separation of ~6 nm in 30 ns long simulations. The external force (F_{ext}) acting on the

862 pull group as the simulation progresses with time (t) is defined by the relation:

863 $$F_{ext} = k\ (vt - x) \tag{5}$$

864 where k is the spring constant, v is the pull velocity, and x is the displacement of the ligand from its

865 initial position. The pull force was applied to COM of Cα atoms of the RING domain (residues 70-109)

866 at a low pull rate of 0.125 nm ns^{-1} (k=1500 kJ mol^{-1} nm^{-2}). The same box dimensions were used as in

867 the case of umbrella sampling. The COM of Cα atoms of UBC13 was kept fixed by periodically

868 removing its rotational and translation motion to promote dissociation of the complex. The cumulative

869 work (W) done to separate complex was calculated using the relation:

870
$$W = \int F \,.dx = 1/2 \sum (f_i + f_{i+1})(x_{i+1} - x_i) \qquad (6)$$

871 The work done over two successive simulation steps (i and i+1) is calculated as a product of the

872 average force (f) multiplied by the displacement of the ligand between the steps. W is thus calculated

873 by numerically integrating the work done between all successive steps of the simulation. The force

874 and COM position of TRAF6^{RING} was recorded every 5 ps. F_{max} (rupture force) is defined as the

875 maximum value of the force recorded in the Force-COM extension profile of an individual or averaged

876 SMD trajectory. W was defined at a COM separation of 4.5 nm in the Work-COM extension profile as

877 all native contacts were found to be disrupted at this COM separation. Both F_{max} and W correlate with

878 the binding affinity of the complex and hence allow for an analysis of the effect of mutations on the

879 stability of the complex.

880

881 **Cloning and mutagenesis**

882 A synthetic construct for TRAF6^{RING} (residues 50-124) was synthesized at Thermo Fischer Scientific,

883 USA. PCR amplified ORF was cloned into a pGEX4T1 vector using NEB HF cloning kit (New England

884 Biolabs, Inc. USA). E69A-TRAF6 was cloned using PCR based site-directed mutagenesis. Variants of

885 UBC13 were generated using PCR based site-directed mutagenesis in WT-UBC13 in pET24 vector (a

886 gift from Prof. Rachel Klevit). RNF38 plasmid was a gift from Prof. Danny Huang. TRAF6^{RZ3} plasmid

887 was a gift from Prof. Catherine Day. All the plasmids were confirmed by sequencing**.**

888

889 **Protein expression and purification**

49

890 All proteins were expressed in BL21 DE3 star cells (Invitrogen), grown at 37°C (in LB media for

891 unlabeled proteins and in M9 media for C-13 or N-15 labeled proteins) till OD_{600} reached 0.7 and were

892 induced with 0.5 mM IPTG for 4-5 hours. The harvested cells were lysed in 50 mM Tris, 250 mM NaCl,

893 5 mM βME, 2% glycerol, 0.01% triton-X, 1 mM PMSF and DNase at pH 7.5 using Emulsiflex high-

894 pressure homogenizer. GST-TRAF6^{RING} and GST-RNF38^{RING} (residues 387-465) were bound to

895 GSTrap HP columns (GE Healthcare) and were eluted with 10 mM reduced glutathione. The proteins

896 were further purified by gel filtration in Superdex 75 pg 16/600 (GE Healthcare) in 25 mM Tris, 100

897 mM NaCl and 5 mM βME at pH 7.5. The His-tagged UBC13 and its variants were bound to HisTrap

898 HP columns (GE Healthcare) and were eluted with 100mM-500mM Imidazole gradient. The proteins

899 were further purified by gel filtration in Superdex 75 pg 16/600 (GE Healthcare) in 25 mM Tris, 100

900 mM NaCl and 5 mM βME at pH 7.5. TRAF6^{RZ3} was induced at OD_{600}~0.7 with 0.2mM IPTG and

901 0.1mM $ZnCl_2$. The lysed cells were resuspended in 50 mM Tris, 350 mM NaCl, 7mM βME, 1 mM

902 PMSF, 10 mg Lysozyme, 0.01% Triton X, pH 8 and centrifuged. The supernatant was bound to

903 HisTrap beads and was with 150mM-450mM Imidazole gradient. The eluent was subsequently

904 purified by gel filtration in Superdex 75 pg 16/600 (GE Healthcare) in 25 mM Tris, 100 mM NaCl and 5

905 mM βME at pH 7.5

906 For the purification of Ub and its variants, lysed cells were resuspended in lysis buffer (50 mM Sodium

907 acetate, 5 mM BME, 0.01% Triton X, pH 4.5), lysed by sonication and centrifuged to pellet cell debris.

908 The supernatant was passed through the SP FF column (GE Healthcare) and the protein was eluted

909 by gradient elution with increasing salt concentration (0 mM NaCl- 600 mM NaCl). The proteins were

910 further purified by gel filtration chromatography on Superdex 75 16/600 column (GE Healthcare) in 50

911 mM Sodium Phosphate, 100 mM NaCl, 5 mM BME, pH 6.5. For the purification of control K63-linked

912 di-Ub, 1 µM UbE1, 40 µM Ubc13, 40 µM GB1-MMS2, 40 µM GST-RNF38, 200 µM D77-Ub and 200

913 µM K63A-Ub were mixed with reaction buffer (50 mM Sodium Phosphate, 5 mM $MgCl_2$, 3 mM ATP,

914 0.5 mM DTT, pH 6.5) overnight. The mixture was dialyzed in 50mM Sodium Acetate, 5mM BME, pH

915 4.5, and centrifuged. The supernatant was passed through the SP FF column (GE Healthcare) and the

50

916 di-Ub was separated by gradient elution with increasing salt concentration (0 mM NaCl- 600 mM

917 NaCl).

918

919 **NMR Spectroscopy**

920 All NMR titration experiments were recorded at 298K on 600 MHz or 800 MHz Bruker Avance III

921 HD spectrometer with a cryoprobe head. The samples were prepared in 25 mM Tris, 100 mM NaCl,

922 pH 7.5, and 10% D_2O. For NMR titration experiments, either ~2 mM TRAF6^{RING} or ~ 1 mM RNF38^{RING}

923 were titrated into ~0.15 mM ^{15}N-UBC13, ^{15}N-dUBC13 and other mutants. The titration data was fit in

924 1:1 protein:ligand model using the equation $CSP_{obs} = CSP_{max} \{([P]_t+[L]_t+K_d) - [([P]_t+[L]_t+K_d)^2-$

925 $4[P]_t[L]_t]^{1/2}\}/2[P]_t$, where $[P]_t$ and $[L]_t$ are total concentrations of protein and ligand at any titration point.

926 The Arginine sidechain spectra of UBC13 and dUBC13 were recorded at 298K on 800 MHz Bruker

927 Avance III HD spectrometer with a cryoprobe head, processed with NMRpipe (Delaglio et al. 1995)

928 and analyzed with Sparky (Kneller & Kuntz 1993). The samples were prepared in 25 mM phosphate,

929 50 mM NaCl, pH 6.0. D_2O was not directly added to the NMR sample to avoid additional signals due to

930 2H isotopomers. For NMR lock, the 3mm NMR tube was inserted co-axially in an external tube

931 containing D_2O. The arginine sidechain Hε, Nε, Cζ resonances were assigned by broadband NOESY-

932 HSQC, HNCACB (Junji Iwahara and Marius Clore, JBNMR 2006), 2D HD(CD)NE and HD(CDNE)CZ

933 (Frans Mulder JACS 2007) experiments.

934

935 ***In-vitro* ubiquitination assay, discharge assay, and Ub$_2$ synthesis assay**

936 For ubiquitination assay using TRAF6^{RZ3}, E1 (0.5 µM), UBC13 and MMS2 (20 µM) and Alexa Fluor

937 Maleimide (Invitrogen) labeled UbS20C (20 µM) were incubated with TRAF6^{RZ3} (15 µM) in UB-buffer

938 (50 mM Tris, 5 mM ATP, 5 mM MgCl$_2$, 20mM NaCl, 2 mM DTT, pH 8) at 37°C for 10 minutes. The

939 same reaction was repeated with GST-TRAF6^{RING} instead of TRAF6^{RZ3}. The reaction mixtures were

940   separated in 12% SDS gel, and the images were acquired in Uvitec (Cambridge). For ubiquitination

941   assay using GST-RNF38^{RING}, E1 (0.5 µM), UBC13 and MMS2 (5 µM) and Alexa Fluor Maleimide

942   (Invitrogen) labeled UbS20C (20 µM) were incubated with GST-RNF38^{RING} (3 µM) in 20 mM Tris, 5

943   mM ATP, 5 mM MgCl$_2$ (pH 7.5) at 37°C for 30 minutes. The reaction mixtures were separated in

944   12%-15% SDS gel, and the images were acquired in iBright FL1000 (Invitrogen). For Ub conjugation

945   assays, E1 (1 µM), UBC13/dUBC13 (20 µM), and K63A-Ub (100 µM) were incubated in UB-buffer at

946   37°C for 15 minutes. For discharge assays, E1 (1 µM), UBC13/dUBC13 (20 µM), and K63A-Ub (100

947   µM) were incubated in UB-buffer at 37°C for 60 minutes. The reaction was quenched with EDTA (30

948   mM) at room temperature for 5 min. MBP-Mms2 (40 µM), TRAF6^{RING} or RNF38^{RING} (40 µM) and

949   Lysine (15 mM) were added to start Ub-discharge. The reaction was quenched by 4X non-reducing

950   SDS loading buffer at desired time-points. For Ub$_2$ synthesis kinetics, E1 (1 µM), UBC13/dUBC13 (20

951   µM), and K63A-Ub (100 µM) were incubated in UB-buffer at 37°C for 60 minutes. The reaction was

952   quenched with EDTA (30 mM) at room temperature for 5 min. Then MBP-Mms2 (40 µM), RNF38^{RING}

953   (40 µM) and D77-Ub (20-100 µM) were added to start Ub$_2$ synthesis. The reaction was quenched by

954   4X non-reducing SDS loading buffer at desired time-points. The reaction mixtures of Ub conjugation,

955   Ub discharge, and Ub$_2$ synthesis were separated in 12% SDS gel, stained overnight with SYPRO

956   Ruby (Invitrogen) and the images were acquired in Uvitec (Cambridge).

957

958   ***In-vitro* binding assay**

959   For the pull-down of TRAF6^{RZ3} with UBC13~Ub conjugate, an Ub conjugation reaction was performed

960   as described above, and the reaction was quenched with EDTA at room temperature for 5 min. MBP-

961   Mms2 (80 µM) was incubated on amylose bead (NEB) in 50 mM Tris, 20mM NaCl, pH 8. The

962   UBC13~Ub conjugate (20 µM) was then mixed with TRAF6^{RZ3} (60 µM) and MBP-Mms2 on the

963   amylose beads for 1 hour at 4°C, washed (3x, each time centrifuged at 3500 rpm for 3 min). After the

964   final wash, the pellet was resuspended in 50 mM Tris, 20mM NaCl, pH 8 and separated on 12% SDS

965   gel. For the pull-down of UBC13~Ub conjugate with GST-RNF38^{RING}, the GST-RNF38^{RING} was

966   incubated with glutathione agarose (Thermo Fisher). The UBC13~Ub conjugate was mixed with GST-

967   RNF38^{RING} (60 µM) on glutathione agarose for 1 hour at 4°C, washed (3x), resuspended in 50 mM

968   Tris, 20mM NaCl, pH 8 and separated on 12% SDS gel. The gels for both pull-down assays were

969   stained overnight with SYPRO Ruby (Invitrogen), and the images were acquired in Uvitec

970   (Cambridge).

971

References

973   Abraham, M.J., Murtola, T., Schulz, R., Páll, S., Smith, J.C., Hess, B. & Lindah, E. 2015, 'Gromacs:
974   High performance molecular simulations through multi-level parallelism from laptops to
975   supercomputers', *SoftwareX*, vol. 1–2, pp. 19–25.

976   Alsallaq, R. & Zhou, H.X. 2008, 'Electrostatic rate enhancement and transient complex of protein-
977   protein association', *Proteins: Structure, Function and Genetics*, vol. 71, no. 1, pp. 320–35.

978   Ashida, H., Kim, M. & Sasakawa, C. 2014, 'Exploitation of the host ubiquitin system by human
979   bacterial pathogens', *Nature Reviews Microbiology*, vol. 12, no. 6, pp. 399–413.

980   Baker, N.A., Sept, D., Joseph, S., Holst, M.J. & McCammon, J.A. 2001, 'Electrostatics of
981   nanosystems: Application to microtubules and the ribosome', *Proceedings of the National
982   Academy of Sciences*, vol. 98, no. 18, pp. 10037–41.

983   Behera, A.P., Naskar, P., Agarwal, S., Banka, P.A., Poddar, A. & Datta, A.B. 2018, 'Structural insights
984   into the nanomolar affinity of RING E3 ligase ZNRF1 for Ube2N and its functional implications',
985   *Biochemical Journal*, vol. 475, no. 9, pp. 1569–82.

986   Berendsen, H.J.C., Postma, J.P.M., Van Gunsteren, W.F., Dinola, A. & Haak, J.R. 1984, 'Molecular
987   dynamics with coupling to an external bath', *The Journal of Chemical Physics*, vol. 81, no. 8, pp.
988   3684–90.

989   Best, R.B. & Hummer, G. 2009, 'Optimized Molecular Dynamics Force Fields Applied to the Helix−Coil
990   Transition of Polypeptides', *The Journal of Physical Chemistry B*, vol. 113, no. 26, pp. 9004–15.

991   Bjelkmar, P., Larsson, P., Cuendet, M. a., Hess, B. & Lindahl, E. 2010, 'Implementation of the
992   CHARMM Force Field in GROMACS: Analysis of Protein Stability Effects from Correction Maps,
993   Virtual Interaction Sites, and Water Models', *Journal of Chemical Theory and Computation*, vol. 6,
994   no. 2, pp. 459–66.

995   Branigan, E., Plechanovová, A., Jaffray, E.G., Naismith, J.H. & Hay, R.T. 2015, 'Structural basis for
996   the RING-catalyzed synthesis of K63-linked ubiquitin chains', *Nature Structural and Molecular
997   Biology*, vol. 22, no. 8, pp. 597–602.

998   Buetow, L., Gabrielsen, M., Anthony, N.G., Dou, H., Patel, A., Aitkenhead, H., Sibbet, G.J., Smith,
999   B.O. & Huang, D.T. 2015, 'Activation of a Primed RING E3-E2-Ubiquitin Complex by Non-
1000   Covalent Ubiquitin', *Molecular Cell*, vol. 58, no. 2, pp. 297–310.

1001 Bussi, G., Donadio, D. & Parrinello, M. 2007, 'Canonical sampling through velocity rescaling', *Journal*
1002   *of Chemical Physics*, vol. 126, no. 1.

1003 Chen, Z.J. 2005, 'Ubiquitin signaling in the NF-κB pathway', *Nature Cell Biology*, vol. 7, no. 8, pp.
1004   758–65.

1005 Christensen, D.E., Brzovic, P.S. & Klevit, R.E. 2007, 'E2–BRCA1 RING interactions dictate synthesis
1006   of mono- or specific polyubiquitin chain linkages', *Nature Structural &Amp; Molecular Biology*, vol.
1007   14, p. 941.

1008 Darden, T., York, D. & Pedersen, L. 1993, 'Particle mesh Ewald: An N ·log(N) method for Ewald
1009   sums in large systems', *The Journal of Chemical Physics*, vol. 98, no. 12, pp. 10089–92.

1010 Das, R., Liang, Y.-H., Mariano, J., Li, J., Huang, T., King, A., Tarasov, S.G., Weissman, A.M., Ji, X. &
1011   Byrd, R.A. 2013, 'Allosteric regulation of E2:E3 interactions promote a processive ubiquitination
1012   machine.', *The EMBO journal*, vol. 32, no. 18, pp. 2504–16.

1013 Das, R., Mariano, J., Tsai, Y.C., Kalathur, R.C., Kostova, Z., Li, J., Tarasov, S.G., McFeeters, R.L.,
1014   Altieri, A.S., Ji, X., Byrd, R.A. & Weissman, A.M. 2009, 'Allosteric Activation of E2-RING Finger-
1015   Mediated Ubiquitylation by a Structurally Defined Specific E2-Binding Region of gp78', *Molecular*
1016   *Cell*, vol. 34, no. 6, pp. 674–85.

1017 Daura, X., Gademann, K., Jaun, B., Seebach, D., van Gunsteren, W.F. & Mark, A.E. 1999, 'Peptide
1018   Folding: When Simulation Meets Experiment', *Angewandte Chemie International Edition*, vol. 38,
1019   no. 1/2, pp. 236–40.

1020 Delaglio, F., Grzesiek, S., Vuister, G.W., Zhu, G., Pfeifer, J. & Bax, A. 1995, 'NMRPipe: A
1021   multidimensional spectral processing system based on UNIX pipes', *Journal of biomolecular*
1022   *NMR*, vol. 6, no. 3, pp. 277–93.

1023 Dou, H., Buetow, L., Sibbet, G.J., Cameron, K. & Huang, D.T. 2012, 'BIRC7-E2 ubiquitin conjugate
1024   structure reveals the mechanism of ubiquitin transfer by a RING dimer', *Nature Structural and*
1025   *Molecular Biology*, vol. 19, no. 9, pp. 876–83.

1026 Dunbrack, R.L. 2002, 'Rotamer Libraries in the 21st Century', *Current Opinion in Structural Biology*,
1027   vol. 12, no. 4, pp. 431–40.

1028 Dunkelberger, E.B., Buchanan, L.E., Marek, P., Cao, P., Raleigh, D.P. & Zanni, M.T. 2012,
1029   'Deamidation accelerates amyloid formation and alters amylin fiber structure', *Journal of the*
1030   *American Chemical Society*, vol. 134, no. 30, pp. 12658–67.

1031 Essmann, U., Perera, L., Berkowitz, M.L., Darden, T., Lee, H. & Pedersen, L.G. 1995, 'A smooth
1032   particle mesh Ewald method', *J Chem Phys*, vol. 103, no. 1995, pp. 8577–93.

1033 Grubm ller, H., Heymann, B. & Tavan, P. 1996, 'Ligand Binding: Molecular Mechanics Calculation of
1034   the Streptavidin-Biotin Rupture Force', *Science*, vol. 271, no. 5251, pp. 997–9.

1035 Hess, B. 2008, 'P-LINCS: A Parallel Linear Constraint Solver for Molecular Simulation', *Journal of*
1036   *Chemical Theory and Computation*, vol. 4, no. 1, pp. 116–22.

1037 Hess, B., Kutzner, C., Van Der Spoel, D. & Lindahl, E. 2008, 'GRGMACS 4: Algorithms for highly
1038   efficient, load-balanced, and scalable molecular simulation', *Journal of Chemical Theory and*
1039   *Computation*, vol. 4, no. 3, pp. 435–47.

1040 Hoefling, M. & Gottschalk, K.E. 2010, 'Barnase-Barstar: From first encounter to final complex', *Journal*
1041   *of Structural Biology*, vol. 171, no. 1, pp. 52–63.

1042 Hornak, V., Abel, R., Okur, A., Strockbine, B., Roitberg, A. & Simmerling, C. 2006, 'Comparison of
1043   multiple Amber force fields and development of improved protein backbone parameters.',
1044   *Proteins*, vol. 65, no. 3, pp. 712–25.

1045 Hub, J.S., De Groot, B.L. & Van Der Spoel, D. 2010, 'G-whams-a free Weighted Histogram Analysis
1046   implementation including robust error and autocorrelation estimates', *Journal of Chemical Theory*
1047   *and Computation*, vol. 6, no. 12, pp. 3713–20.

1048 Jorgensen, W.L., Chandrasekhar, J., Madura, J.D., Impey, R.W. & Klein, M.L. 1983, 'Comparison of
1049   simple potential functions for simulating liquid water', *The Journal of Chemical Physics*, vol. 79,
1050   no. 2, pp. 926–35.

1051 Joung, I.S. & Cheatham, T.E. 2008, 'Determination of alkali and halide monovalent ion parameters for
1052   use in explicitly solvated biomolecular simulations', *Journal of Physical Chemistry B*, vol. 112, no.
1053   30, pp. 9020–41.

1054 Kneller, D.G. & Kuntz, I.D. 1993, 'UCSF Sparky: An NMR Display, Annotation and Assignment Tool',
1055   *Journal of Cellular Biochemistry*, vol. 53 (S17C), p. 254.

1056 Komander, D. & Rape, M. 2012, 'The Ubiquitin Code', *Annual Review of Biochemistry*, vol. 81, no. 1,
1057   pp. 203–29.

1058 Kumar, S., Rosenberg, J.M., Bouzida, D., Swendsen, R.H. & Kollman, P.A. 1992, 'The Weighted
1059   Histogram Analysis Method for Free-energy calculations on biomolecules. I. The Method', *Journal*
1060   *of Computational Chemistry*, vol. 13, no. 8, pp. 1011–21.

1061 Lindorff-Larsen, K., Piana, S., Palmo, K., Maragakis, P., Klepeis, J.L., Dror, R.O. & Shaw, D.E. 2010,
1062   'Improved side-chain torsion potentials for the Amber ff99SB protein force field', *Proteins:*
1063   *Structure, Function and Bioinformatics*, vol. 78, no. 8, pp. 1950–8.

1064 Matsuzawa, S. -i., Reed, J.C., Fukushima, T., Lefebvre, S., Ronai, Z., Krajewska, M., Bruey, J.M.,
1065   Kress, C.L. & Zapata, J.M. 2007, 'Ubiquitin-conjugating enzyme Ubc13 is a critical component of
1066   TNF receptor-associated factor (TRAF)-mediated inflammatory responses', *Proceedings of the*
1067   *National Academy of Sciences*, vol. 104, no. 15, pp. 6371–6.

1068 Meireles, L. n.d., *ANCHOR: A Webserver and Database for Analysis of Protein-Protein Interaction*
1069   *Hotspots for Drug Discovery*, viewed <http://structure.pitt.edu/anchor/>.

1070 Metzger, M.B., Hristova, V.A., Weissman, A.M. & Es, R. 2010, 'HECT and RING finger families of E3
1071   ubiquitin ligases at a glance', *Journal of cell science*, vol. 125, no. 5, pp. 531–7.

1072 Middleton, A.J., Budhidarmo, R., Das, A., Zhu, J., Foglizzo, M., Mace, P.D. & Day, C.L. 2017a, 'The
1073   activity of TRAF RING homo- and heterodimers is regulated by zinc finger 1', *Nature*
1074   *Communications*, vol. 8, no. 1, p. 1788.

1075 Middleton, A.J., Budhidarmo, R., Das, A., Zhu, J., Foglizzo, M., Mace, P.D. & Day, C.L. 2017b, 'The
1076   activity of TRAF RING homo-and heterodimers is regulated by zinc finger 1', *Nature*
1077   *Communications*, vol. 8, no. 1, pp. 1–10.

1078 Moreira, I.S., Fernandes, P.A. & Ramos, M.J. 2007, 'Hot spots-A review of the protein-protein
1079   interface determinant amino-acid residues', *Proteins: Structure, Function, and Bioinformatics*, vol.

1080   68, no. 4, pp. 803–12.

1081   Pan, A.C., Jacobson, D., Yatsenko, K., Sritharan, D., Weinreich, T.M. & Shaw, D.E. 2019, 'Atomic-
1082   level characterization of protein–protein association', *Proceedings of the National Academy of*
1083   *Sciences*, vol. 116, no. 10, pp. 4244–9.

1084   Pande, A., Mokhor, N. & Pande, J. 2015, 'Deamidation of Human γS-Crystallin Increases Attractive
1085   Protein Interactions: Implications for Cataract', *Biochemistry*, vol. 54, no. 31, pp. 4890–9.

1086   Parrinello, M. & Rahman, A. 1981, 'Polymorphic transitions in single crystals: A new molecular
1087   dynamics method', *Journal of Applied Physics*, vol. 52, no. 12, pp. 7182–90.

1088   Peters, M.B., Yang, Y., Wang, B., Füsti-Molnár, L., Weaver, M.N. & Merz, K.M. 2010, 'Structural
1089   survey of zinc-containing proteins and development of the zinc AMBER force field (ZAFF)',
1090   *Journal of Chemical Theory and Computation*, vol. 6, no. 9, pp. 2935–47.

1091   Pettersen, E.F., Goddard, T.D., Huang, C.C., Couch, G.S., Greenblatt, D.M., Meng, E.C. & Ferrin, T.E.
1092   2004, 'UCSF Chimera---A visualization system for exploratory research and analysis', *Journal of*
1093   *Computational Chemistry*, vol. 25, no. 13, pp. 1605–12.

1094   Plechanovov, A., Jaffray, E.G., Tatham, M.H., Naismith, J.H. & Hay, R.T. 2012, 'Structure of a RING
1095   E3 ligase and ubiquitin-loaded E2 primed for catalysis', *Nature*, vol. 489, no. 7414, pp. 115–20.

1096   Pruneda, J.N., Littlefield, P.J., Soss, S.E., Nordquist, K. a, Chazin, W.J., Brzovic, P.S. & Klevit, R.E.
1097   2012, 'Structure of an E3:E2~Ub complex reveals an allosteric mechanism shared among
1098   RING/U-box ligases.', *Molecular cell*, vol. 47, no. 6, pp. 933–42.

1099   Qin, S., Pang, X. & Zhou, H.X. 2011, 'Automated prediction of protein association rate constants',
1100   *Structure*, vol. 19, no. 12, pp. 1744–51.

1101   Ribet, D. & Cossart, P. 2010, 'Post-translational modifications in host cells during bacterial infection',
1102   *FEBS Letters*, vol. 584, no. 13, pp. 2748–58.

1103   Sanada, T., Kim, M., Mimuro, H., Suzuki, M., Ogawa, M., Oyama, A., Ashida, H., Kobayashi, T.,
1104   Koyama, T., Nagai, S., Shibata, Y., Gohda, J., Inoue, J.I., Mizushima, T. & Sasakawa, C. 2012,
1105   'The Shigella flexneri effector OspI deamidates UBC13 to dampen the inflammatory response',
1106   *Nature*, vol. 483, no. 7391, pp. 623–6.

1107   Schilder, J. & Ubbink, M. 2013, 'Formation of transient protein complexes', *Current Opinion in*
1108   *Structural Biology*, vol. 23, no. 6, pp. 911–8.

1109   Schreiber, G., Haran, G. & Zhou, H.-X. 2009, 'Fundamental Aspects of Protein−Protein Association
1110   Kinetics', *Chemical Reviews*, vol. 109, no. 3, pp. 839–60.

1111   Selzer, T., Albeck, S. & Schreiber, G. 2000, 'Rational design of faster associating and tighter binding
1112   protein complexes', *Nature Structural Biology*, vol. 7, no. 7, pp. 537–41.

1113   Skinner, J.J., Wang, S., Lee, J., Ong, C., Sommese, R., Sivaramakrishnan, S., Koelmel, W.,
1114   Hirschbeck, M., Schindelin, H., Kisker, C., Lorenz, K., Sosnick, T.R. & Rosner, M.R. 2017,
1115   'Conserved salt-bridge competition triggered by phosphorylation regulates the protein
1116   interactome', *Proceedings of the National Academy of Sciences*, p. 201711543.

1117   Soss, S.E., Yue, Y., Dhe-Paganon, S. & Chazin, W.J. 2011, 'E2 conjugating enzyme selectivity and
1118   requirements for function of the E3 ubiquitin ligase CHIP', *Journal of Biological Chemistry*, vol.

1119   286, no. 24, pp. 21277–86.

1120   Tang, C., Iwahara, J. & Clore, G.M. 2006, 'Visualization of transient encounter complexes in protein–
1121   protein association', *Nature*, vol. 444, no. 7117, pp. 383–6.

1122   Torrie, G.M. & Valleau, J.P. 1977, 'Nonphysical sampling distributions in Monte Carlo free-energy
1123   estimation: Umbrella sampling', *Journal of Computational Physics*, vol. 23, no. 2, pp. 187–99.

1124   Volkov, A.N., Bashir, Q., Worrall, J.A.R., Ullmann, G.M. & Ubbink, M. 2010, 'Shifting the equilibrium
1125   between the encounter state and the specific form of a protein complex by interfacial point
1126   mutations', *Journal of the American Chemical Society*.

1127   Wang, L., Siu, S.W.I., Gu, W. & Helms, V. 2010, 'Downhill binding energy surface of the barnase-
1128   barstar complex', *Biopolymers*, vol. 93, no. 11, pp. 977–85.

1129   Washington, E.J., Banfield, M.J. & Dangl, J.L. 2013, 'What a difference a Dalton makes: bacterial
1130   virulence factors modulate eukaryotic host cell signaling systems via deamidation.', *Microbiology*
1131   *and molecular biology reviews : MMBR*, vol. 77, no. 3, pp. 527–39.

1132   van Wijk, S.J.L., Melquiond, A.S.J., de Vries, S.J., Timmers, H.T.M. & Bonvin, A.M.J.J. 2012,
1133   'Dynamic Control of Selectivity in the Ubiquitination Pathway Revealed by an ASP to GLU
1134   Substitution in an Intra-Molecular Salt-Bridge Network', *PLoS Computational Biology*, vol. 8, no.
1135   11.

1136   van Wijk, S.J.L., de Vries, S.J., Kemmeren, P., Huang, A., Boelens, R., Bonvin, A.M.J.J. & Timmers,
1137   H.T.M. 2009, 'A comprehensive framework of E2-RING E3 interactions of the human ubiquitin-
1138   proteasome system.', *Molecular systems biology*, vol. 5, no. 295, p. 295.

1139   Yin, Q., Lin, S.C., Lamothe, B., Lu, M., Lo, Y.C., Hura, G., Zheng, L., Rich, R.L., Campos, A.D.,
1140   Myszka, D.G., Lenardo, M.J., Darnay, B.G. & Wu, H. 2009, 'E2 interaction and dimerization in the
1141   crystal structure of TRAF6', *Nature Structural and Molecular Biology*, vol. 16, no. 6, pp. 658–66.

1142   Yoo, J. & Aksimentiev, A. 2012, 'Improved Parametrization of Li + , Na + , K + , and Mg 2+ Ions for All-
1143   Atom Molecular Dynamics Simulations of Nucleic Acid Systems', *The Journal of Physical*
1144   *Chemistry Letters*, vol. 3, no. 1, pp. 45–50.

1145   Yoo, J. & Aksimentiev, A. 2016a, 'Improved Parameterization of Amine-Carboxylate and Amine-
1146   Phosphate Interactions for Molecular Dynamics Simulations Using the CHARMM and AMBER
1147   Force Fields', *Journal of Chemical Theory and Computation*, vol. 12, no. 1, pp. 430–43.

1148   Yoo, J. & Aksimentiev, A. 2016b, 'Refined Parameterization of Nonbonded Interactions Improves
1149   Conformational Sampling and Kinetics of Protein Folding Simulations', *Journal of Physical*
1150   *Chemistry Letters*, vol. 7, no. 19, pp. 3812–8.

1151   Yoshimura, Y., Oktaviani, N.A., Yonezawa, K., Kamikubo, H. & Mulder, F.A.A. 2017, 'Unambiguous
1152   Determination of Protein Arginine Ionization States in Solution by NMR Spectroscopy',
1153   *Angewandte Chemie International Edition*, vol. 56, no. 1, pp. 239–42.

1154   Zhao, J., Li, J., Xu, S. & Feng, P. 2016, 'Emerging Roles of Protein Deamidation in Innate Immune
1155   Signaling', *Journal of Virology*, vol. 90, no. 9, pp. 4262–8.

1156   Zhu, X. & Mitchell, J.C. 2011, 'KFC2: A knowledge-based hot spot prediction method based on
1157   interface solvation, atomic density, and plasticity features', *Proteins: Structure, Function and*
1158   *Bioinformatics*, vol. 79, no. 9, pp. 2671–83.

1159